

# Transfer learning from first-principles calculations to experiments with chemistry-informed domain transformation

Yuta YAHAGI<sup>1,2</sup>, Kiichi OBUCHI<sup>1,2</sup>, Fumihiko KOSAKA<sup>2</sup> and Kota MATSUI<sup>3</sup>

<sup>1</sup> NEC Corporation, Minato-ku, Tokyo, Japan, 108-8001

<sup>2</sup> National Institute of Advanced Industrial Science and Technology, Tsukuba, Japan, 305-8568

<sup>3</sup> Nagoya University, Nagoya, Japan, 466-8550

E-mail: yuta-yahagi@nec.com

January 2025

**Abstract.** Simulation-to-Real (Sim2Real) transfer learning, the machine learning technique that efficiently solves a real-world task by leveraging knowledge from computational data, has received increasing attention in materials science as a promising solution to the scarcity of experimental data. We proposed an efficient transfer learning scheme from first-principles calculations to experiments based on the chemistry-informed domain transformation, that integrates the heterogeneous source and target domains by harnessing the underlying physics and chemistry. The proposed method maps the computational data from the simulation space (source domain) into the space of experimental data (target domain). During this process, these qualitatively different domains are efficiently bridged by prior knowledge of chemistry, the statistical ensemble and the relationship between source and target quantities.

As a proof-of-concept, we predict the catalyst activity for the reverse water-gas shift reaction by using the abundant first-principles data in addition to the experimental data. Through the demonstration, we confirmed that the transfer learning model exhibits positive transfer in accuracy and data efficiency. In particular, a significantly high accuracy was achieved despite using a few (less than ten) target data in domain transformation, whose accuracy is one order of magnitude smaller than that of a full scratch model trained with over 100 target data. This result indicates that the proposed method leverages the high prediction performance with few target data, which helps to save the number of trials in real laboratories.

## 1. Introduction

Machine learning (ML) is now a driving force for innovation in a broad range of industries fueled by the explosive growth of deep learning (DL) technologies. Beyond the traditional three paradigms of science, theory, experiment and computation, data science has emerged as a fourth paradigm of science [1]. ML has paved the way not only

for advanced information processing, but also for data-driven approaches in real-world challenges such as material development [2, 3, 4, 5].

In practice, the data-driven approach for materials often fails because of the lack of real data. Experimental data in materials science are scarce and non-scalable due to several reasons: (1) the high cost and time required for synthesis and measurement; (2) the disparate modality depending on measurement methods; and (3) the exploration bias, where the data collected is biased towards known or easily accessible regions of the material space, making ML tasks extrapolate beyond existing data. Although there are attempts to obtain large datasets by running high-throughput experiments [6, 7, 8, 9, 10], combinatorial synthesis [11, 12, 13, 14, 15], and laboratory automation [16, 17, 18], the available materials and conditions are limited, and the data sizes are still insufficient, typically of the order of  $O(100)$ , below the requirement of common DL methods.

On the other hand, computational data generated by first-principles calculations such as density functional theory (DFT) have been increasingly used in the context of ML. Compared to real experiments, numerical computations are scalable and easily automated, providing a large and abundant dataset. Such computational datasets obtained by high-throughput DFT calculations are available in a wide variety of materials [19, 20, 21, 22, 23, 24, 25]. However, computational data also has limitations. Computational methods rely on several approximations and assumptions, and thus systematic errors must appear in the results. The impact of such errors on predictions in reality cannot be known without comparison with experiments. Although it is sometimes possible to reproduce reality by performing high-fidelity calculations, such calculations are often expensive and significantly degrade its data throughput. Therefore, computational and experimental data are complementary to each other in which the former is lower cost but lower fidelity and the other is *vice versa*, motivating the introduction of transfer learning. Such a transfer scheme, called the Sim2Real (Simulation-to-Real) transfer, has been successfully introduced in some areas [26, 27, 28, 29].

Although it is reasonable to hypothesize that the Sim2Real transfer is also effective for material discovery, this is challenging due to the fundamental differences between first-principles calculations and real experiments. The most fatal issue is the difference in the scales: a first-principles calculation provides a microscopic description of a single (often simple) structure, which is represented by a set of atoms; an experimental measurement captures a macroscopic profile of a composite of various structures distributed near thermal equilibrium, which is usually difficult to control or even characterize.

Kinetics is also a serious issue. To predict the kinetics of a real system, one needs to find the most plausible process among all combinations of possible elementary processes, which is explosive. Moreover, evaluation of a single elementary process is still expensive, as it requires a series of calculations to find a minimum energy path between an initial and a final state. For instance, let us consider the case of thermal catalysis on a solid-state surface [30]. A single first-principles calculation can provide a snapshot of an

adsorption process on a simple periodic surface; it is far from a real experiment that measures a reaction rate resulting from the entire reaction path on a complex surface, involving various facets, surface reconstructions, and catalyst-support interactions.

The central challenge addressed in this study is to bridge the gap between first-principles calculations and experiments, enabling Sim2Real transfer for material design. We propose a novel Sim2Real transfer method based on a chemistry-informed domain transformation that uses the laws of underlying physics and chemistry. The proposed method consists of two steps. It first transforms the domain of source computational data into that of target experimental data through formulas obtained in theoretical chemistry. Then, it solves the problem as homogeneous transfer learning, which can be easily solved with common transfer learning methods. If the domain transformation is chemically appropriate and satisfies the transfer assumptions in the homogeneous domain [31, 32], a positive transfer can be expected in the second step. Ultimately, this approach allows us to build a predictive model that leverages the best of both worlds: the scalability and low cost of large-scale computational data while correcting for systematic errors using experimental data.

This paper is organized as follows. Section 2 reviews related works in the field of Sim2Real transfer and transfer learning for materials. Section 3 describes the proposed method in detail. Section 4 demonstrates the effectiveness of the proposed method through a case study on catalyst activity prediction. Section 5 discusses the results and potential future directions. Finally, Section 6 concludes the paper with a summary of the findings and their implications.

In summary, the key contributions of this work are as follows:

- **A novel Sim2Real transfer framework for materials:** We introduce a new transfer learning method using chemistry information that effectively tackles the challenges of data scarcity.
- **Practical application to catalyst discovery:** We predict catalyst activity using the proposed method, paving the way for practical applications.
- **Positive transfer:** Extensive experiments using real data confirmed the positive transfer improving accuracy and data efficiency, underscoring the effectiveness of our approach in practical scenarios.

## 2. Related works

### 2.1. Simulation-to-Real (Sim2Real) Transfer

Sim2Real transfer, the process of transferring knowledge from simulations to real-world applications, has been extensively studied in various fields such as computer vision, robotics, and some experimental sciences. Data generation and model training in simulation spaces can be conducted at a lower cost compared to real-world scenarios. However, there exists a gap between the simulator and the real world, which often serves as a major cause of failure when transferring data or models to real-world applications.

This gap can arise, for instance, from inconsistencies in physical parameters (e.g., friction, damping, mass, density) or inaccuracies in physical modeling. Bridging the gap between simulation and the real world requires improving the simulation environment to better approximate reality. To achieve this, various approaches have been extensively studied, including system identification [26], which builds mathematical models of the physical system serving as the simulator; domain adaptation [27, 28], which adjusts the distribution of simulation data to align with real-world data; and domain randomization [29], which generates diverse pseudo-domains with randomized properties and trains models to perform robustly across all of them. In this study, we do not focus on reconstructing the simulator itself, making system identification an unsuitable approach. Additionally, domain randomization requires performing simulations under numerous randomized settings, which would necessitate a large-scale computational environment when combined with high-cost simulations such as the DFT calculations targeted in this work. Therefore, we focus on domain adaptation, which can be achieved at a relatively lower computational cost.

## 2.2. Transfer learning in Materials Science

In the context of materials science, Sim2Real transfer is gaining traction as a promising approach to address the scarcity of experimental data. For instance, Jha *et al.* [33] proposed a parameter transfer scheme from DFT datasets to a target dataset based on a neural network model. They successfully built a highly accurate model for predicting formation energy, which is significantly better than the predictive models built using only DFT datasets. Wu *et al.* [34] proposed a Sim2Real transfer method to predict the thermal conductivity of polymers by transferring parameters learned in the source task predicting specific heat capacity with computational data. They demonstrated that the target task can benefit from the source task, achieving high accuracy with limited experimental data. Han and Choi also attempted a Sim2Real transfer to predict the NMR chemical shift from the computed magnetic shielding constant [35]. Vermeire and Green applied a Sim2Real transfer approach to the solvation free energies leveraging a large computational dataset of solvent/solute combinations [36]. Aoki *et al.* [37] developed a multitask learning framework of Flory–Huggins  $\chi$  parameters for polymer-solvent systems. Their method integrates computational data with biased experimental data, enabling a highly generalized model to be applicable to a wider area than the coverage of experimental data.

Data assimilation is a related approach to combine computational and experimental data. Harashima *et al.* [38] proposed a data assimilation method in which a small number of experimental data and a large number of computational data are integrated. They applied this method to the search for permanent magnet compositions and succeeded in finding candidates that exhibit good properties at finite temperatures despite using few experimental data at finite temperatures with computational data limited to zero temperature.

In a similar sense to Sim2Real transfer, multi-fidelity transfer learning from abundant computational data to expensive but accurate ones is also a promising approach. Smith *et al.* [39] provided highly accurate neural network potential by training a network to DFT data, then retraining to more accurate coupled cluster calculation data. Ju *et al.* [40] performed a feature-based transfer learning for predicting the lattice thermal conductivity of crystalline materials leveraging the scattering phase space data as a source data. Both properties are obtained from first-principles calculations, but the former is more expensive to compute than the latter. They demonstrated that feature transfer from the source task can significantly improve the prediction accuracy of the target task.

Shim *et al.* uses transfer learning to predict reaction conditions for new nucleophiles in Pd-catalyzed cross-coupling reactions. By combining transfer learning with active learning, the research efficiently identifies reaction conditions, successfully accelerating the discovery of chemical reactions [41].

Although there are many successful examples of transfer learning in materials science as listed above, these methods assume similar domains between the source and target where either feature space or target variable is identical; It is still challenging to integrate computational and experimental data across heterogeneous domains, which is the focus of this study.

### 2.3. Physics/Chemistry-Informed Machine Learning

Physics-informed machine learning integrates physical laws such as differential equations into machine learning models to improve their generalization and performance [42]. In material science, for example, Arora *et al.* [43] proposed a prediction model for the spatio-temporal evolution of deformation in elastic-viscoplastic materials by designing a physics-informed loss function, achieving high accuracy without increasing computational complexity.

Similarly, chemistry-informed machine learning leverages chemical laws, which are mainly based on thermodynamics and statistical mechanics. Bradford *et al.* [44] developed a prediction model for ionic conductivity in polymer electrolytes based on a chemistry-informed neural network. Their architecture incorporates the Arrhenius equation in the final layers, which describes the temperature-activated processes, leading to a significant improvement. Ballard *et al.* [45] performed machine learning modeling for polymerization processes with a chemistry-informed neural network. They incorporate the knowledge of kinetic models into the loss function, resulting in an improved model outperforming conventional ones.

This study, named chemistry-informed domain transformation, can also be regarded as a form of physics/chemistry-informed machine learning. While these previous studies incorporate the knowledge of physical and chemical laws into the models directly, our method uses it to establish some relation between heterogeneous domains for transfer learning, which is a unique challenge in this field.

### 3. Method: Chemistry-informed domain transformation

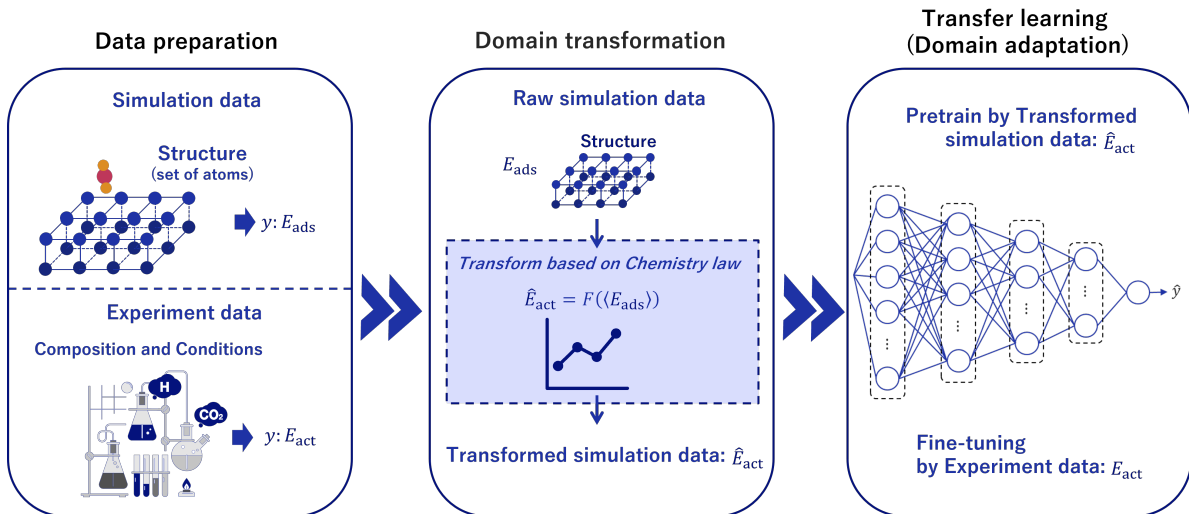


**Figure 1.** Schematics of our Sim2Real transfer learning framework for materials. Here, as an example, the adsorption energy  $E^{\text{ads}}$  and activation energy  $E^{\text{act}}$  are assigned as computational and experimental quantities, respectively. See main text for further explanation.

#### 3.1. Overview

The proposed method consists of two stages, a domain transformation part and a transfer learning part. Since the latter part is a standard set-up on a homogeneous domain adaptation, we focus on the former part.

Let us begin with an overview of the process flow, schematically illustrated in Figure 1. Our method takes as input two distinct datasets: a computational dataset composed of pairs of structures (set of atoms) and computed values (e.g. adsorption energy  $E^{\text{ads}}$ ), and an experimental dataset consisting of pairs of experimental conditions (used in synthesis and measurement) and experimental values (e.g. activation energy  $E^{\text{act}}$ ). Experimental conditions are typically provided as numerical values; transfer learning requires the computational dataset to be converted into the identical format.

To realize the domain transformation, this method leverages a couple of chemical information: the statistical ensemble under which the system follows, and the relational expression between the computational and experimental quantities, such as empirical rules or theoretical formulations, depicted as  $F$ .

The domain transform part first establishes a correspondence between the structures and the conditions through evaluating the ensemble average, which allows us to aggregate all computational data under given conditions, forming the same feature space for the two domains. Then the (averaged) computational quantity is aligned with the experimental quantity with  $F$ . Eventually, it results in the transformed simulation

data in the same domain as the experimental data, enabling homogeneous domain adaptation, a standard situation in transfer learning. We refer to this procedure as the ‘‘Chemistry-informed Domain Transform.’’

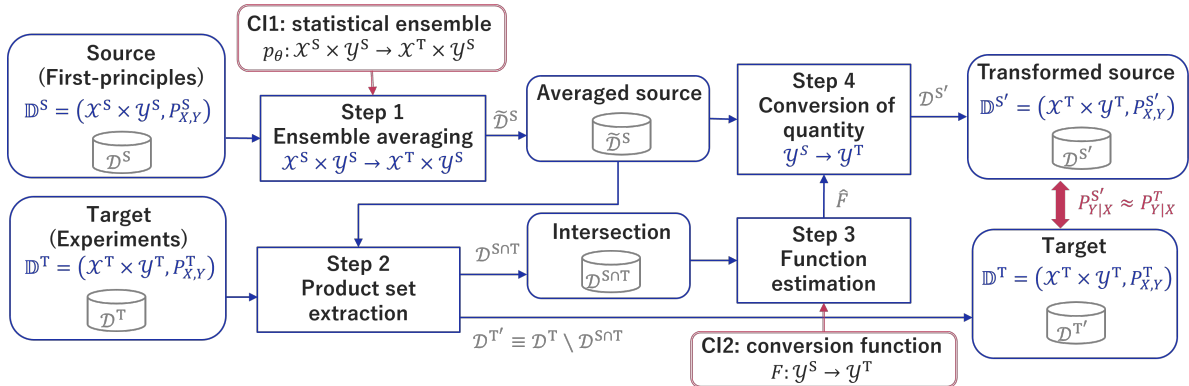


**Figure 2.** Schematics of the chemistry-informed domain transformation. The rectangle box represent the process, rounded rectangle represent the data and its domain, the doubled-rounded rectangle represents the chemical information (CI), respectively.

### 3.2. Domain transformation procedure

We next show a detailed procedure of the chemistry-informed domain transformation as shown in Figure 2. Let the domain be  $\mathbb{D}^r \equiv (\mathcal{X}^r \times \mathcal{Y}^r, P^r_{X,Y})$  with the feature space  $\mathcal{X}^r$ , the output space  $\mathcal{Y}^r$ , and the joint probability distribution  $P^r_{X,Y}$  where  $r = S$  or  $T$  represent the source and target domain, respectively. Then the domain transformation aims to construct transformation rules for the source domain as follows:

$$\mathbb{D}^S = (\mathcal{X}^S \times \mathcal{Y}^S, P^S_{X,Y}) \rightarrow \mathbb{D}^{S'} = (\mathcal{X}^T \times \mathcal{Y}^T, P^{S'}_{X,Y}). \quad (1)$$

If such transformation rules are obtained, we can treat the source domain data (i.e., computational data) as target domain data (i.e., experimental data).

The source data  $\mathcal{D}^S = \{(x_i^S, y_i^S)\}_{i=1}^{N_S}$  is assumed to be obtained from first-principles calculations with the data size  $N_S$ , where  $x^S = \{(\mathbf{r}_a; Z_a)\}_{a=1}^{N_a} \in \mathcal{X}^S$  is a structure, a set of  $N_a$  atoms in certain positions  $\mathbf{r}$  with elemental labels  $Z \in \text{PeriodicTable} = \{\text{H, He, Li, ...}\}$ . Furthermore,  $y^S \in \mathcal{Y}^S$  is a physical quantity accessible from the calculations and correlated with the target measurement. The target data  $\mathcal{D}^T = \{(x_i^T, y_i^T)\}_{i=1}^{N_T}$  are obtained from experiments, where  $x^T \in \mathcal{X}^T$  is an experimental condition, such as chemical composition, temperature, pressure, etc., and  $y^T \in \mathcal{Y}^T$  is a physical quantity measured in the experiments.  $N_T$  is the data size of the target data, assumed to be  $N_T \ll N_S$ .

Here, we additionally introduce the chemistry information (CI):

**CI.1 Statistical ensemble**  $p_\theta$ : a statistical ensemble under which the system follows.

**CI.2 Conversion function  $F$ :** a relationship between quantities as a form of  $F : \mathcal{Y}^S \rightarrow \mathcal{Y}^T$ .

The domain transformation is achieved by following 4 steps:

- (i) **Ensemble averaging:**  $(\mathcal{X}^S \times \mathcal{Y}^S \rightarrow \mathcal{X}^T \times \mathcal{Y}^S)$ .
- (ii) **Product set extraction.**
- (iii) **Function estimation.**
- (iv) **Conversion of quantity:**  $(\mathcal{Y}^S \rightarrow \mathcal{Y}^T)$ .

These procedures result in  $\mathbb{D}^S \rightarrow \mathbb{D}^{S'} \approx \mathbb{D}^T$ , reducing the problem to a homogeneous domain shift. In particular, from the construction of the domain transformation, if the output space  $\mathcal{Y}$  is perfectly aligned, it is expected that the relationship known as covariate shift [31] will hold between the transformed computational data and the experimental data. That is, we can expect that the relation  $P_{Y|X}^{S'} \approx P_{Y|X}^T$  approximately holds. Covariate shift is a typical model for the discrepancy between different domains, and various correction methods have been proposed in machine learning community [46, 47]. By utilizing these methods, it is possible to achieve effective learning of prediction models under the covariate shift.

While we assume a single source domain in the following discussion for simplicity, the same methodology can be applied to multiple source domains with extending  $F : (\mathcal{Y}^S)^d \rightarrow \mathcal{Y}^T$  where  $d$  is the number of sources. Furthermore, there are no specific constraints on the dimensions of  $x^S, x^T$  and  $y^S$ .

**3.2.1. Ensemble averaging:** We first transform the feature space as  $\mathcal{X}^S \times \mathcal{Y}^S \rightarrow \mathcal{X}^T \times \mathcal{Y}^S$ . The objective of this step is to obtain projected source data in the target feature space,  $\tilde{\mathcal{D}}^S = \{(x^{S'}, \tilde{y}^S)\}$  where  $(x^{S'}, \tilde{y}^S) \in \mathcal{X}^T \times \mathcal{Y}^S$ . Here,  $x^{S'} \in \mathcal{X}^T$  is an auxiliary variable with the same feature space as  $x^T$ .  $\tilde{y}^S \in \mathcal{Y}^S$  is the ensemble average of  $y^S$  associated with  $x^{S'}$ :

$$\tilde{y}^S \equiv \mathbb{E}_{x^S}[y^S(x^S)|x^{S'}] \simeq \sum_{x^S} p_\theta(x^S|x^{S'}) y^S(x^S), \quad (2)$$

where  $p_\theta(x^S|x^{S'})$  denotes an occurrence probability of a structure  $x^S$  under a condition  $x^{S'}$  with additional fixed conditions  $\theta$ , that is identical to a statistical ensemble in the context of statistical mechanics.

The form of  $p_\theta(x^S|x^{S'})$  can be immediately determined from the assumed situation. For example, in the case of varying the temperature, Eq. (2) becomes:

$$p(x^S|x^{S'}) \propto \exp \left[ -\frac{E(x^S)}{k_B x^{S'}} \right], \quad (3)$$

where  $k_B$  is the Boltzmann constant,  $E(x^S)$  is the energy of  $x^S$ . This is known as the canonical ensemble. As an advanced example, let us consider the case of varying



the chemical composition under isothermal conditions. In this case,  $x^{S'}$  is a chemical composition and  $\theta = T$  is the fixed temperature, leading:

$$p_T(x^S|x^{S'}) \propto \delta(x^S \in x^{S'}) \exp \left[ -\frac{E(x^S)}{k_B T} \right], \quad (4)$$

where  $\delta(x^S \in x^{S'})$  is a Kronecker delta function that is 1 if a structure  $x^S$  has the composition of  $x^{S'}$  and 0 otherwise.

To evaluate Eq. (2), we need to sample  $x^S$  and compute  $y^S$  with  $E(x^S)$ . This is usually accomplished by running a molecular dynamics or a Monte Carlo simulation with a given  $x^{S'}$ , but it is computationally expensive and sometimes infeasible. In practice, further approximations will be used depending on the available source dataset  $\mathcal{D}^S$ , as demonstrated in the following section. Alternatively,  $\tilde{y}^S$  can be obtained directly with calculations of physical properties or its surrogate model, if available.

**3.2.2. Product set extraction:** After ensemble averaging, we can now compare  $\tilde{\mathcal{D}}^S = \{(x^{S'}, \tilde{y}^S)\}$  with  $\mathcal{D}^T = \{(x^T, y^T)\}$ . As the next step, we arrange a product set of them with respect to  $x^{S'}$  and  $x^T$ , referred as an intersection dataset:

$$\mathcal{D}^{S \cap T} \equiv \{(\tilde{y}_i^S, y_j^T) \mid x_i^{S'} = x_j^T\}_{(i,j)} \subset \mathcal{Y}^S \times \mathcal{Y}^T, \quad (5)$$

whose size is  $N_{S \cap T} \leq N_T$ . This dataset provides a direct comparison between the source and target quantity, and is used in the following step to determine a map of  $\tilde{y}^S$  onto  $\mathcal{Y}^T$ .

To avoid leakage in future steps, the residual target data

$$\mathcal{D}^{T'} = \mathcal{D}^T \setminus \mathcal{D}^{S \cap T} \equiv \{(x_i^T, y_i^T) \mid y_i^T \notin \mathcal{D}^{S \cap T}\}_i, \quad (6)$$

are kept separately.

**3.2.3. Function estimation:** In this work, we assume that there exists a conversion function  $F : \mathcal{Y}^S \rightarrow \mathcal{Y}^T$  from a source quantity to a target one. This  $F$  describes some relation between  $\tilde{y}^S$  and  $y^T$ . It may be either a black box function, an analytic function, or a non-parametric function, depending on the problem. The goal of this step is to estimate  $F$  by using  $\mathcal{D}^{S \cap T}$ .

This task can potentially be solved efficiently by leveraging prior knowledge of the underlying physical and chemical principles. In certain combinations of  $\tilde{y}^S$  and  $y^T$ , the form of  $F$  and its parameter ranges can be deduced by the relevant formulas, such as the theoretical equation, the phenomenological relation and the natural laws. Note that since the sample size  $N_{S \cap T}$  is generally limited, estimating the transformation function  $F$  using a complex model may result in unstable outcomes. In other words, it is important to use the simplest possible model consistent with physical and chemical principles.

As a practical example, we will show a case of catalyst reaction, where the source quantity is the adsorption energy, and the target quantity is the activation energy. In this case, based on the theoretical chemistry, we can deduce that  $F$  is a linear scaling function, which is discussed in detail in the next section.

In addition to domain transformation, another important role of conversion with  $F$  is to correct for systematic errors introduced by the approximations used in the various steps, such as first-principles calculations and ensemble averaging. These errors are finally absorbed into the parameters of  $\hat{F}$  estimated from real data, complementing the fidelity of source data within the capacity of  $F$ .

**3.2.4. Conversion of quantity:** Finally, we convert  $\tilde{y}^S \in \mathcal{Y}^S$  to  $y^{S'} \in \mathcal{Y}^T$  with the estimated function  $\hat{F}$ , resulting in the source data in a transformed domain  $\mathbb{D}^{S'} = \{(\mathcal{X}^T, \mathcal{Y}^T, P_{X,Y}^{S'})\}$ . Since  $F(\tilde{y}_i^S)$  and  $y_j^T$  follow the same distribution for  $x_i^{S'} = x_j^T$  and true  $F$ , we can expect the covariate shift  $P_{Y|X}^{S'} \approx P_{Y|X}^T$  hold approximately if the domain transformation is successful. Now it is ready to perform the homogeneous domain adaptation from  $\mathbb{D}^{S'}$  to  $\mathbb{D}^T$ .

## 4. Demonstration

In this section, we demonstrate the effectiveness of the proposed method through a practical case study on catalyst activity prediction for the reverse water gas shift (RWGS) reaction [48, 49]. We first describe the background and significance of this task. Then, we present the datasets used in this demonstration, followed by designing the task-specific model employing hypotheses appropriate to this situation. Finally, we show the results and implications.

### 4.1. Catalyst activity prediction for RWGS

Catalysts are substances that improve the rate of chemical reactions by mediating them, and they can promote chemical reactions permanently without consuming themselves. They are indispensable to the chemical industry because they enable the production of important chemical substances faster, in larger quantities, and with less energy. The reverse water gas shift (RWGS) reaction is a crucial process in the chemical industry, where  $\text{CO}_2$  is converted to  $\text{CO}$ , an ingredient in a variety of chemical products [48, 49]. The development of novel catalysts has long been an area of interest within the field of chemical engineering.

One of the most widely discussed performance metrics is the activation energy, which is the height of the energy barrier that must be overcome for a chemical reaction to proceed. By developing catalysts with lower activation energies, it is possible to produce products with lower energy and higher efficiency. In particular, for thermochemical catalysts, the operating temperature of the reactor can be lowered, increasing the flexibility of the overall design of the catalytic process. In experimental measurements, the activation energy can be estimated from the formation rate of the product, which requires significant time and human resources.

On the other hand, from the computational perspective, the activation energy cannot be computed directly because it requires the knowledge of the entire reaction

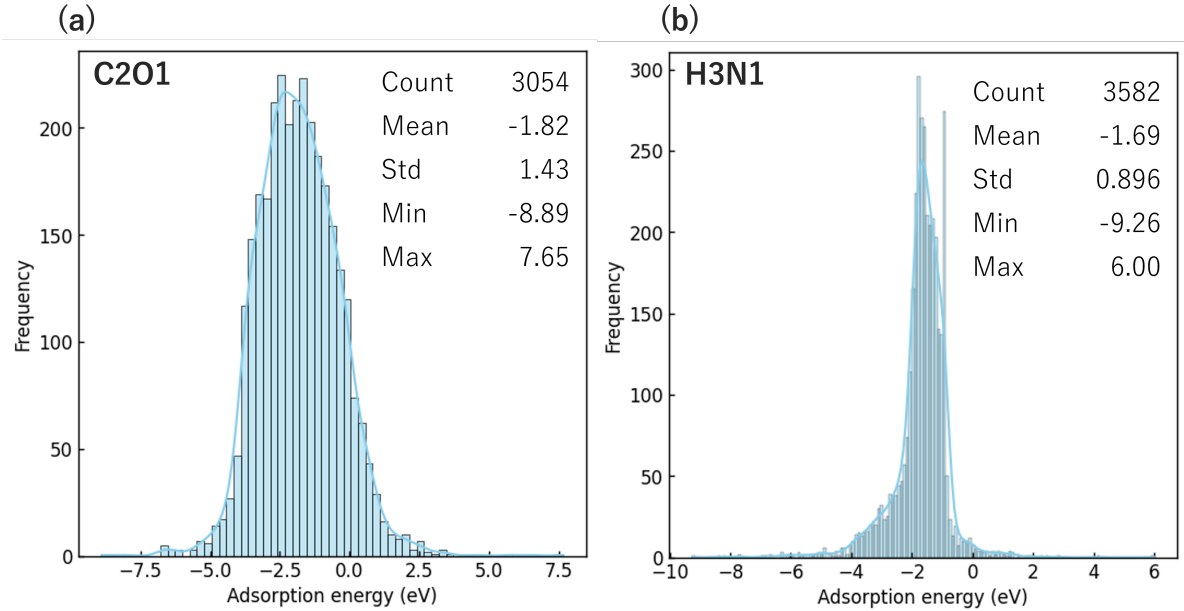


**Figure 3.** Histograms of source data (*OC20*) with (a) C2O1 and (b) H3N1

path, which is computationally unfeasible. Instead, first-principles calculations commonly provide the adsorption energy, the binding energy between an adsorbate and a catalyst surface, which is relatively easy to obtain from structural relaxation [50]. Although this quantity is closely related to the activation energy, they are qualitatively different because the adsorption process is only a part of the total reaction process.

There are two types of quantities, the activation energy that is difficult to obtain but directly related to the target task, and the adsorption energy that is easy to obtain but indirectly related to that. Therefore, this task is a suitable candidate for applying Sim2Real transfer with our method.

#### 4.2. Datasets

Throughout this study, we use the *Open Catalyst 2020 (OC20)* [22], a simulation dataset based on density functional theory (DFT), as a source computational dataset. It presents 48 datasets labeled with the adsorbate (=adsorption molecule)  $M$ ; Each of them is a large collection of pairs of a slab structure  $x^{S(M)}$  and an adsorption energy  $y^{S_M}$  per adsorbate  $M$ . Overall, it includes approximately  $10^6$  entries of  $\sim 2000$  structures  $\times$  48 adsorbates. Figure 3 plots histograms of  $y^S$  from  $\mathcal{D}^{S(\text{C2O1})}$  and  $\mathcal{D}^{S(\text{H3N1})}$  for example. Preparation details are explained in Appendix A.1

Regarding a target dataset, we refer to a high-throughput experimental dataset opened by Wang *et al.* [9], referred to *Wang2023*. Their dataset provides 300 pairs of a catalyst composition  $x^T$  and an activation energy  $y^T$ . Here, we disregard the compositions including lanthanoids as they exceed the coverage of the *OC20*, reducing the data size from 300 to 141. Its histogram is shown in Figure 4. The distribution is

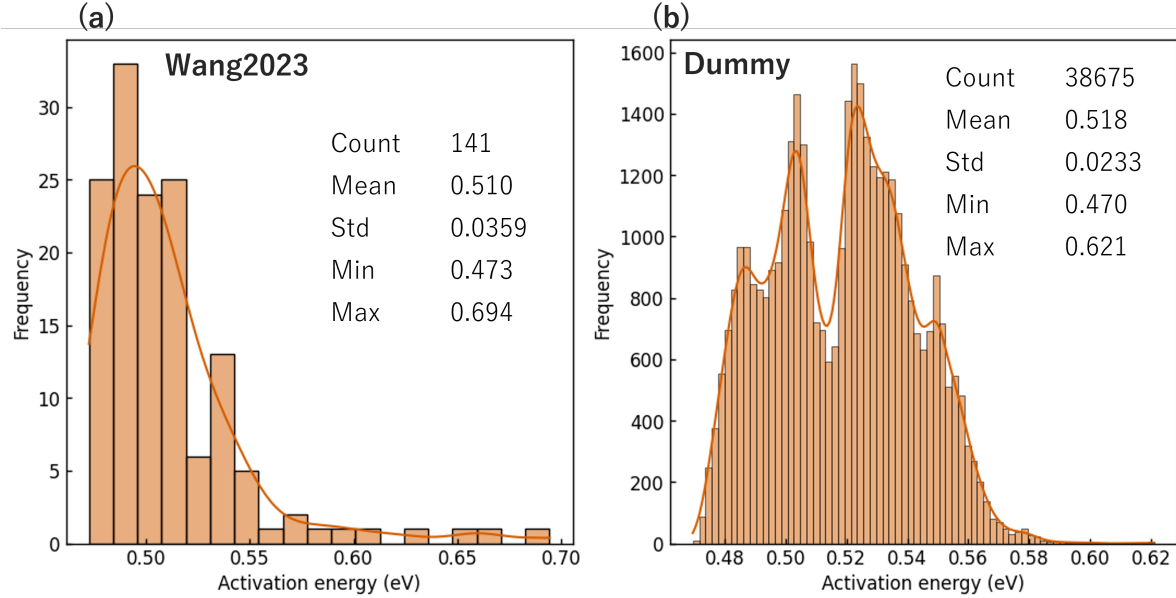


**Figure 4.** Histograms of target data with (a) real experimental data (*Wang2023*) and (b) the dummy data.

around the mean 0.510 with a standard deviation of 0.0359, but also has a tail in the high energy region over 0.55. Preparation details are explained in Appendix A.2

In addition, to verify the effectiveness of our method, we generated a dataset  $\mathcal{D}^{\text{Ta}}$  with 38,674 pseudo-labeled data. It is prepared based on *Wang2023*. Figure 4 provides a histogram of the dummy data, showing a two-peak-like distribution between 0.470 and 0.621 with a standard deviation of 0.0233. The procedure for generating the dummy is given in the Appendix A.3.

#### 4.3. Domain transformation

We now proceed with domain transformation while specifying each step in Sec. 3.2 for this catalyst activity prediction task. Details are explained as follows. Note here that *OC20* is treated as a multiple source in this work.

**4.3.1. Ensemble averaging:** We first perform ensemble averaging for each  $\mathcal{D}^{\text{S}(M)}$  to obtain  $\tilde{\mathcal{D}}^{\text{S}(M)} = \{(x^{\text{S}'}, \tilde{y}^{\text{S}(M)})\} \subset \mathcal{X}^{\text{T}} \times \mathcal{Y}^{\text{S}}$ . Formally, the statistical ensemble can be a probability distribution of surface adsorption structures  $x^{\text{S}}$  arising from a catalyst represented by the composition  $x^{\text{S}'}$  at an operating temperature  $T$ , like Eq. (4).

In this work, however, we approximately consider

$$\tilde{y}^{\text{S}(M)}(x^{\text{S}'}) = \min\{y_i^{\text{S}(M)} \mid x_i^{\text{S}(M)} \text{ has } x^{\text{S}'}\}_i, \quad (7)$$

where "has" in the right-hand side means that a structure  $x_i^{\text{S}}$  has the composition of  $x^{\text{S}'}$ . This is because the phase space of the adsorption structures is enormous to sample and thus requires simplification.

Note that, Eq. (7) corresponds to the low-temperature limit of Eq. (4); In other words, this is nothing more than hypothesizing the following expression for the statistical ensemble:

$$(\text{CI.1}) \quad p \propto \lim_{T \rightarrow +\infty} \delta(x^{S(M)} \in x^{S'(M)}) \exp \left\{ \frac{E(x^{S(M)})}{k_B T} \right\}. \quad (8)$$

Clearly, this is an overly bold approximation that deviates from the actual experimental conditions, and the sample size is insufficient for reliably exploring a minimal  $y^{S(M)}$ , leading to significant systematic errors. However, these approximation errors may be partially mitigated in the subsequent function estimation step.

**4.3.2. Product set extraction:** We then extract the product sets  $\{\mathcal{D}^{S(M) \cap T}\}$  for each  $M$  from  $\{\tilde{\mathcal{D}}^{S(M)}\}$  and  $\mathcal{D}^T$ . To measure the similarity between two compositions, we define:

$$d(x^A, x^B) = \sum_{Z=\text{H,He,Li},\dots}^{\text{PeriodicTable}} |c_Z(x^A) - c_Z(x^B)|, \quad (9)$$

where  $c_Z(x)$  is the concentration of element  $Z$  in a composition  $x$ . Let  $\alpha$  be a threshold, we obtain the product sets as

$$\mathcal{D}^{S(M) \cap T} = \{(\tilde{y}_i^{S(M)}, y_j^T) \mid d(x_i^{S'}, x_j^T) < \alpha\}_{(i,j)}. \quad (10)$$

Here, we assume  $\alpha = 0.3$  for *Wang2023*.

The product sets with the dummy dataset,  $\mathcal{D}^{S(M) \cap T_d}$ , are obtained similarly, but assuming  $\alpha = 0.05$  due to the denseness of  $\mathcal{D}^{T_d}$ .

To avoid data leakage, subtracted target datasets

$$\mathcal{D}^{T'(M)} = \mathcal{D}^T \setminus \mathcal{D}^{S(M) \cap T} \equiv \{(x_i^T, y_i^T) \mid y_i^T \notin \mathcal{D}^{S(M) \cap T}\}_i, \quad (11)$$

are defined and used in the subsequent domain adaptation process. The number of  $N_{S(M) \cap T}$  depends on  $M$ , but is in the range of 10 to 13 for each  $\mathcal{D}^{S(M) \cap T}$ . The precise values will be summarized later (See Table 3).

**4.3.3. Function estimation:** Next, we estimate a conversion function from adsorption energies to an activation energy,  $F : (\mathcal{X}^S)^d \rightarrow \mathcal{Y}$ , where it is a many-to-one mapping reflecting the multi-source situation. A form of  $F$  can be deduced by referring to the empirical rule known as the Brønsted–Evans–Polanyi (BEP) relation [51, 30]:

- (i) In many cases, catalytic activity is determined by a rate-determining step (RDS) in the reaction path. Thus, only limited adsorbates related to the RDS are sufficient for consideration.
- (ii) There is a linear correlation between the activation energy and the adsorption energy on the RDS,

leading the following expression:

$$(C1.2) \quad F(\tilde{\mathbf{y}}^S) = a_{M^*} \tilde{\mathbf{y}}^{S(M^*)} + b_{M^*}, \quad (12)$$

where  $\tilde{\mathbf{y}}^S \equiv \{\tilde{y}^{S(M)}\}_M$  is a vector obtained by concatenating  $\tilde{y}^{S(M)}$  over all sources,  $M^*$  is an adsorbate selected among the sources.  $a_{M^*}$  and  $b_{M^*}$  are the coefficient and intercept of linear regression with  $\mathcal{D}^{S(M^*)}$ . Comparing the form of  $F$  to the BEP relation, selecting  $M^*$  corresponds to the first law: Ideally,  $M^*$  should be selected as the adsorbate involved in the RDS. The assumption of linear scaling immediately corresponds to the second law.

Estimation of  $F$  is performed by multiple steps of source selection that determine  $M^*$  and linear regression that determines  $a_{M^*}$  and  $b_{M^*}$ , as presented in Algorithm 1. While there are various methods for source selection, in this work we consider the two types of selection strategies:

- S1. Prior knowledge of kinetics:** Selection of a source associated with any one of the reaction intermediates of RWGS.
- S2. Regression performance to the BEP relation:** Selection of a source that fit well with the activation energies in linear regression.

The strategy S1 treats  $M^*$  as a sort of chemical information and selects it empirically. In the case of the RWGS reaction, the possible intermediates involved in RDS are CO, HCOO and COOH [52]; There is no exact match to these in the *OC20*, the adsorbates listed in Table 1 are possible candidates for close matches.

Contrary, the S2 strategy is a hybrid of chemistry-informed and data-driven;  $M^*$  is selected from the sources that well describe the linear scaling. A source selection algorithm with this strategy is shown in Algorithm 2. In order to perform source selection while dealing with data misalignment during integration, we adopt an algorithm combining the multiple imputation with variable selection, proposed by Wood, White, and Royston [53]. Here, we refer to the occurrence frequency through iterations of multiple imputation as a criterion for source selection.

---

**Algorithm 1:** Function estimation for  $\hat{F}$ .

---

**Input:**  $\{\mathcal{D}^{S(M) \cap T}\}_M$ : Intersection data,  $F$ : Conversion function

**Output:**  $\hat{F}$ : Conversion function with estimated parameters.

```

1 begin
2    $M^* \leftarrow \text{SourceSelection}(\{\mathcal{D}^{S(M) \cap T}\}_M);$ 
3    $\hat{a}_{M^*}, \hat{b}_{M^*} \leftarrow \text{LinearRegression}(\mathcal{D}^{S(M^*) \cap T});$ 
4    $\hat{F}(\tilde{\mathbf{y}}^S) \leftarrow \hat{a}_{M^*} \times \tilde{\mathbf{y}}^{S(M^*)} + \hat{b}_{M^*};$ 
5   return  $\hat{F}$ ;

```

---

Applying the Algorithm 2 to  $\{\mathcal{D}^{S(M) \cap T}\}_M$ , Figure 5 displays the adsorbates whose occurrence frequency exceeds 50%. Theirs linear regression lines are shown in Figure 6,

**Table 1.** List of adsorbates (= label of sources) selected for each strategy.

Strategy	Selected adsorbates
S1	C2O1, H1C2O1, H1C2O2, H1C2O2, H2C2O1, H2C2O2
S2 ( <i>Wang2023</i> )	H3C1, H3C2, H5C2O2, H3C2O1, H3N1, H1O1, H1N1O1
S2 (dummy)	H5C2O1, N2O1, H3C2, H1C2O1, H4C2O2, C1, H2C1, H3C2O1, H3N1

---

**Algorithm 2:** Source selection with multiple-imputation method.

---

**Input:**  $\{\mathcal{D}^{S(M) \cap T}\}_M$ : Intersection data,  $F$ : Conversion function

**Output:**  $f^{\text{occ}}$ : Occurrence frequency of each source among iteration.

**parameter:**  $N_{\text{imp}}$ : Times of imputation iteration,  $\lambda$ : regularization coefficient.

**1 begin**
**2**     $\mathcal{D}^{\text{Join}} \leftarrow \text{OuterJoin}(\{\mathcal{D}^{S(M) \cap T}\}_M);$ 
**3**    Standerize  $\mathcal{D}^{\text{Join}}$ ;

**4**     $f^{\text{occ}} \leftarrow \mathbf{0};$ 
**5**    **for**  $i = 1$  **to**  $N_{\text{imp}}$  **do**
**6**         $\mathcal{D}^{\text{Imputed}} \leftarrow \mathcal{D}^{\text{Join}};$ 
**7**        Missing data in  $\mathcal{D}^{\text{Imputed}} \leftarrow \mathcal{N}(0, 1)$ : Normal distribution;

**8**         $\hat{\mathbf{W}}^{\text{LASSO}} \leftarrow \text{LASSO}(\mathcal{D}^{\text{Imputed}}; \lambda);$ 
**9**        **for**  $M$  **do**
**10**            **if**  $\hat{W}_M^{\text{LASSO}} \neq 0$  **then**
**11**                 $f_M^{\text{occ}} \leftarrow f_M^{\text{occ}} + 1;$ 
**12**    **return**  $f^{\text{occ}};$ 


---

presenting different lines depending on the sources. We consider these to be candidate sources and expect any one of them to give an adequate conversion. The selected sources from the strategy S2 are summarized in Table. 1. Detailed results and numerical values of the function estimation are given in Appendix C.1.

Because the linear regression fits to the target data, some unanticipated effects and approximation errors may be mitigated within a capacity of  $F$ , thereby complementing the low fidelity of the simulations.

Note that, while we rely on the linear scaling between activation and adsorption energy, this simple relation breaks down in certain cases, known as the Sabatier's principle [54]. This principle states that the adsorption energy should not be too strong or too weak, since it follows a volcano curve. To capture this behavior, more representative functions such as a piecewise linear function can be used as the form of  $F$ , which is beyond the scope of this paper.

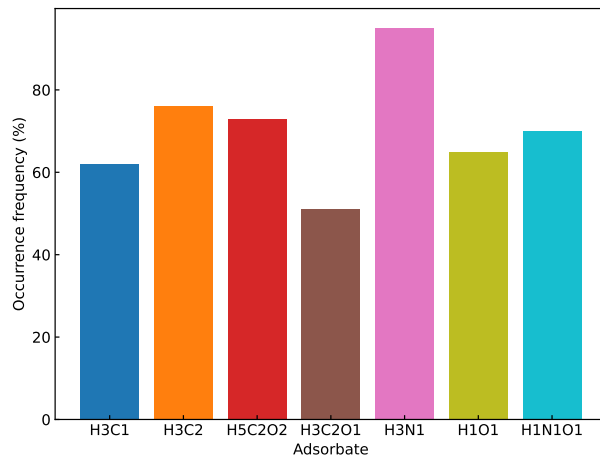


**Figure 5.** Occurrence frequency during iteration in the multiple imputation.

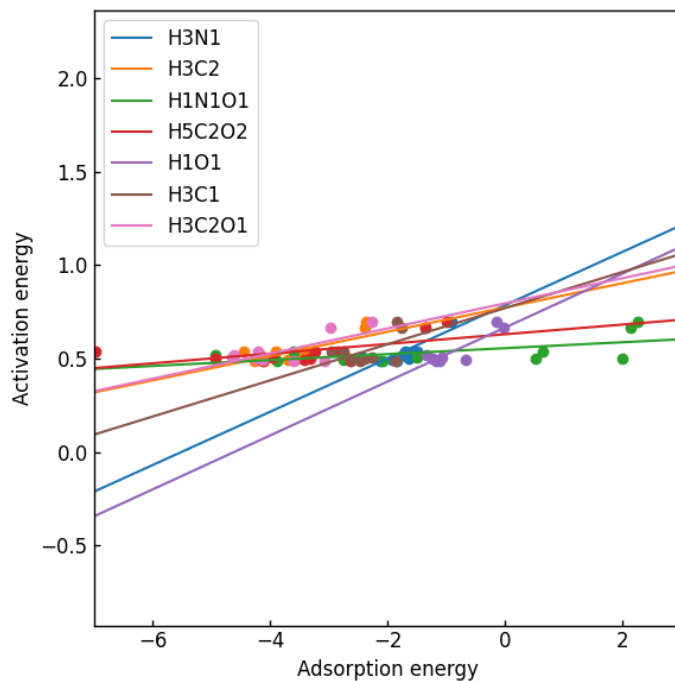


**Figure 6.** Linear regression of activation energy by adsorption energy of the sources selected with S2 strategy.

**4.3.4. Conversion of physical quantity:** We convert  $\hat{\mathbf{y}}_i^S$  to  $y^{S'}$  with the estimated function  $\hat{F}$ , resulting in source data on the target space  $\mathcal{D}^{S'} = \{(x^{S'}, y^{S'})\}$ , with the transformed source domain,  $\mathbb{D}^{S'} = (\mathcal{X}^T \times \mathcal{Y}^T, P_{X,Y}^{S'})$ . Figures 7 compare the label distribution of the transformed source data ( $P(Y^{S'})$ ) and target data ( $P(Y^T)$ ) for *Wang2023* and the dummy data, respectively. In all Adsorbates, the transformed source distribution is closer in shape to the target distribution than the raw *OC20*



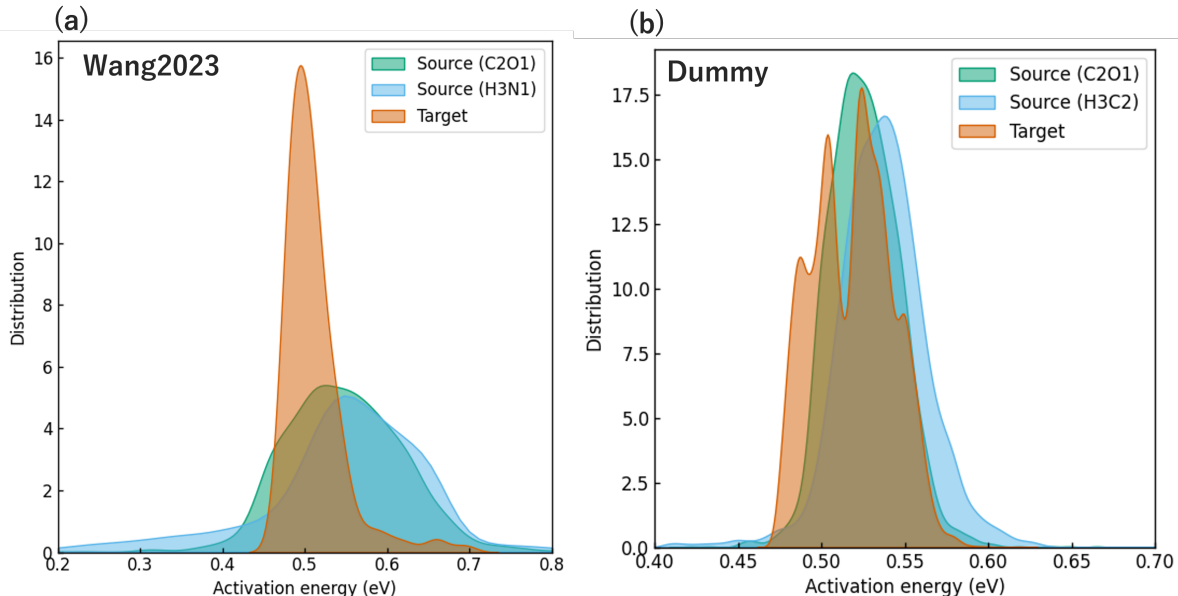


**Figure 7.** Comparison of the converted source distributions and the target distribution of (a) *Wang2023* and (b) dummy. The density distributions are estimated with a kernel density estimation method.

**Table 2.** Wasserstein distances between the raw or transformed source and target (*Wang2023* or the dummy) distributions.

	Raw source (C2O1)	Transformed source (C2O1)
<i>Wang2023</i>	1.012	0.8727
Dummy	1.043	0.2161

distributions in Figures 7. Furthermore, to quantitatively evaluate the effectiveness of our domain transformation, we calculated the discrepancy between distributions of the source and target domain before and after the transformation using the Wasserstein distance [55]. The Wasserstein distance can be interpreted as a measure of the cost required to transform one probability distribution into another and a smaller Wasserstein distance suggests that the two distributions are closer to each other. Table 2 shows the Wasserstein distances between the source (C2O1) distribution and the target distribution, suggesting that the distributions are closer to each other by domain transformation.

**4.3.5. Homogeneous transfer learning:** Finally, transfer learning pert performs the homogeneous domain adaptation. For input of the model, the composition is converted into the chemical descriptors generated by the *XenonPy* code [56]. We employ 224 descriptors that is relevant to our problem out of 290 descriptor, shown in Appendix Appendix B. These descriptors are standardized using all compositions in *OC20* dataset.

The prediction model is based on a fully connected neural network (FCNN) model

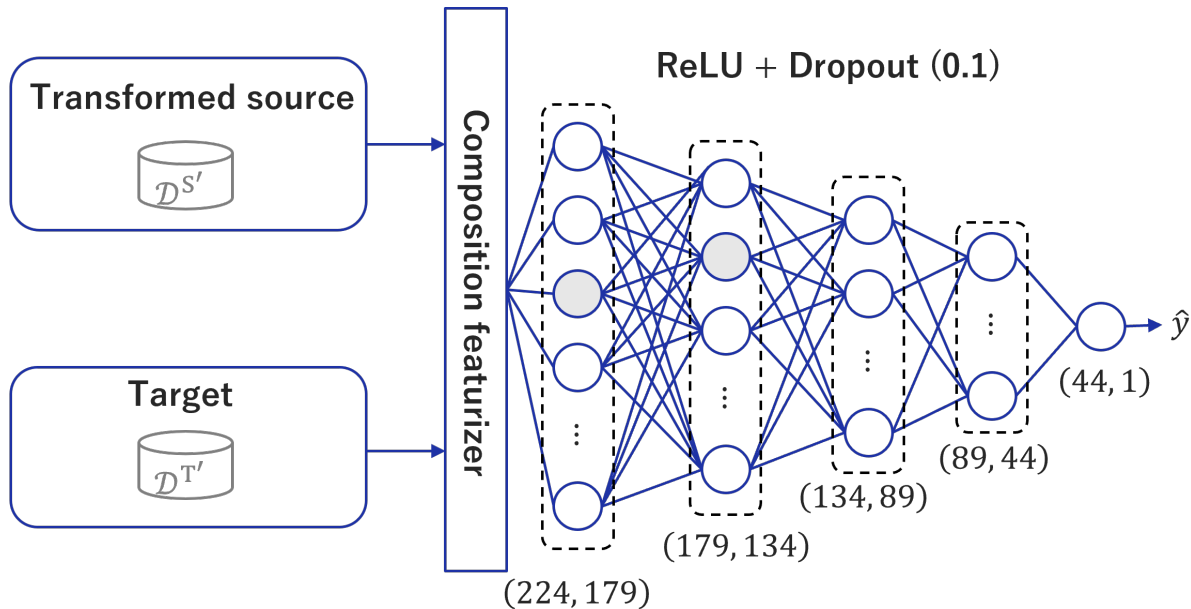


**Figure 8.** Architecture of the neural network prediction model.

with five layers, as shown in Figure 8. The number of units in each layer gradually decreases, starting from the input dimension 224, in the first layer, followed by 179, 134, 89, and 44, in the middle layers, with the final output layer having one unit. All units are activated by ReLU (rectified linear unit) and applied dropout at a rate of 0.1. It should be noted that a similar five-layer FCNN architecture with compositional descriptors has already been successfully used in a previous study [40].

To train a prediction model, we first prepare a source model from  $\mathcal{D}^S$ . With the target training, we compare two different methods: the fine-tuning (FT) that re-optimizes all layers, and the transfer learning (TL) that fixes the middle layers and retrain only the final layer. During both training phases, the parameters are optimized so as to minimize the loss of mean squared error by the stochastic gradient descent algorithm with 32 batches with learning rate = 0.001, which is implemented in the PyTorch framework [57].

#### 4.4. Training

We constructed a prediction model according to the method shown in Section 4.3.5. After domain transformation, the source model was trained using  $\mathcal{D}^S$ , then the prediction models were prepared by retraining the source model on  $\mathcal{D}^{T'}$ . Here, we use 80% of the target data for retraining and separate the remaining 20% as the test data. Training for dummy target data proceeds similarly. More details of the training are presented in Appendix C.

#### 4.5. Performance evaluation

In this section, we present the evaluation results of the prediction model based on test error measurements, with a focus on learning efficiency. The performance evaluation is structured into two parts: validation using dummy data and practical assessment using real *Wang2023* data.

The effects of Sim2Real transfer were measured by evaluating the test loss as a function of the target training data size. Figure 9 shows the result of dummy target data pretrained with *OC20* (C2O1) dataset selected by S1 strategy. Here, we evaluate the mean loss and its standard deviation in five trials in which data were randomly selected from the training data set in each trial.

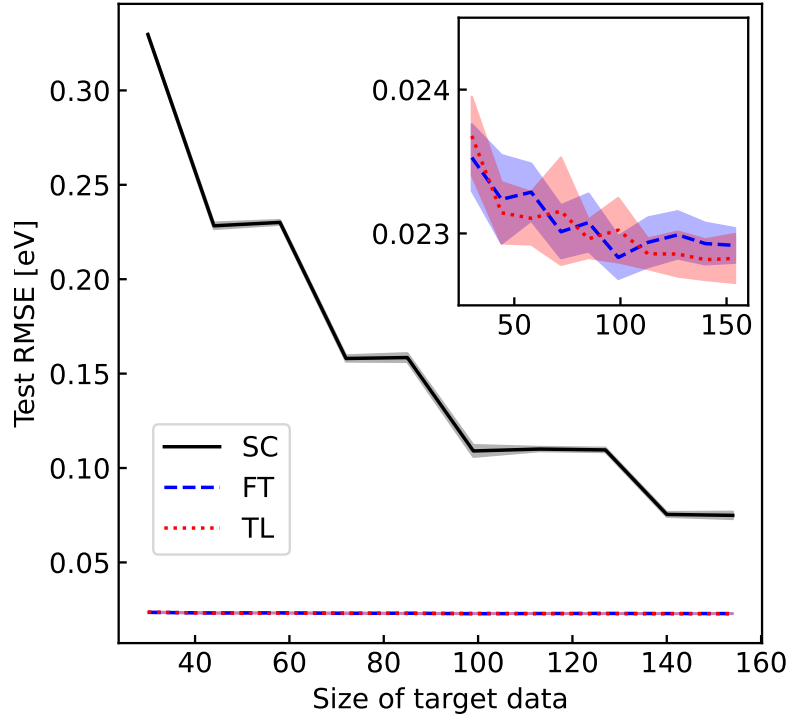


**Figure 9.** Prediction accuracy measured by the test root mean squared error as a function of the size of used training data (a) with and (b) without the full-scratch model. The black solid line represents the full-scratch (SC) model, the blue dashed line the fine-tuning (FT), and the red dotted line the transfer-learning(TL), respectively (See main text). The hatched area represents the standard deviation in five trials.

*4.5.1. Verification with dummy data:* Compared to the case of the scratch model (trained with target data only), the transferred model clearly reduces the prediction error by approximately one order of magnitude. This is a direct evidence of positive transfer. Furthermore, the losses of transferred models have been minimized even without the

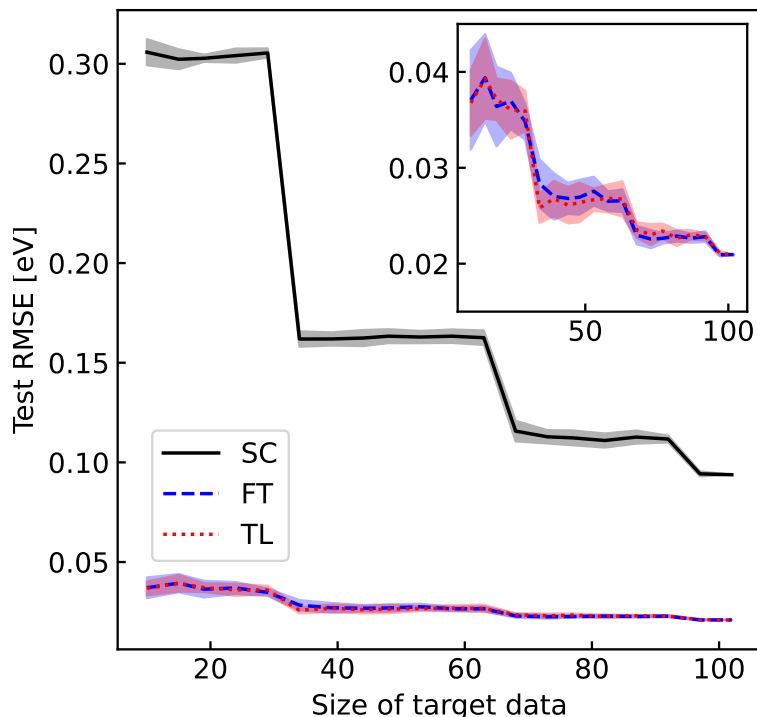


**Figure 10.** Test error as a function of the size of training target data similar to Figure 9.

target training steps, indicating that the source model has almost converged on optimal parameters in the target space. In comparison with the FT and the TL, there is little difference.

*4.5.2. Demonstration with real data:* Next, let us evaluate performances for real experimental data from *Wang2023* by using the pretrained model with *OC20* (C2O1) dataset. We also find positive transfer in this case from Figure 10, indicating approximately 1/10 of the error reduction by knowledge transfer. Compared to Figure 9, the error at the start is higher, but still be lower than any value of the loss of scratch model; Thus, the transferred knowledge provides near-optimal parameters on the target domain. Similar to the previous section, the FT and the TL show almost same performance.

*4.5.3. Comparison of source datasets:* At the end of this section, we will investigate source data dependencies. Since transfer method does not affect the model performance as shown in above, TL is used in this section.

We evaluated the performances of transferred model for different source datasets in *OC20* selected with the strategy S1 or S2, summarized in Table 3. Figure 11 shows the

**Table 3.** Summary of transfer learning with different source data.

Source $M$	Strategy	$N_{S(M)\cap T}$	Pretrain error (eV)	Final error (eV)
C2O1	S1	12	0.05869	0.02088
H3N1	S2	13	0.04875	0.02253
H1C2O2	S1	11	0.02573	0.02333
H1C2O1	S1	13	0.07309	0.02456
H3C1	S2	12	0.06917	0.02473
H3C2O1	S2	13	0.08887	0.02498
H1N1O1	S2	13	0.06496	0.02768
H3C2	S2	13	0.10224	0.02786
H5C2O2	S2	12	0.05854	0.02835
H2C2O2	S1	13	0.06268	0.03262
H2C2O1	S1	13	0.06956	0.03293
H1O1	S2	10	0.04391	0.03849

model performance for some of the sources included in the table. This result indicates that the final test errors depends on the source selection, however, transferred model performs enough better than the scratch model regardless of the used source. Although C2O1 from S1 strategy performs relatively better in terms of final accuracy, H3N1 from S2 strategy reaches similar accuracy.

It should be emphasized here that the frequency of occurrence from the S2 strategy (Figure 5) does not necessarily correspond to the performance of the transferred with the selected source. This is because the BEP relation claims that the activation energy can be linearly regressed on the adsorption energy of a molecule related to the RDS, but the converse is not true. Therefore, the source selection shown in Algorithm. 2 is a procedure for exploring candidates rather than selecting the best one.

#### 4.6. Discussions

Let us discuss the implications of the results and future perspectives.

Our demonstrations in both a dummy dataset and a real dataset indicate that the proposed method successfully transfers the knowledge from source computational datasets beyond the domain gap, enabling highly efficient learning on the target real-world task. Pretraining with transformed source data, using only a few ( $\sim 10$ ) target data for domain transformation, shows a significant improvement in prediction accuracy with reducing test losses one order of magnitude.

Moreover, the results show that the transferred knowledge gives nearly optimal parameters in target model, suggesting a potential to reduce a number of experiments required to develop prediction models for novel catalysts.

Although the current study demonstrates the potential of the proposed method, there are several areas for future improvement and exploration.

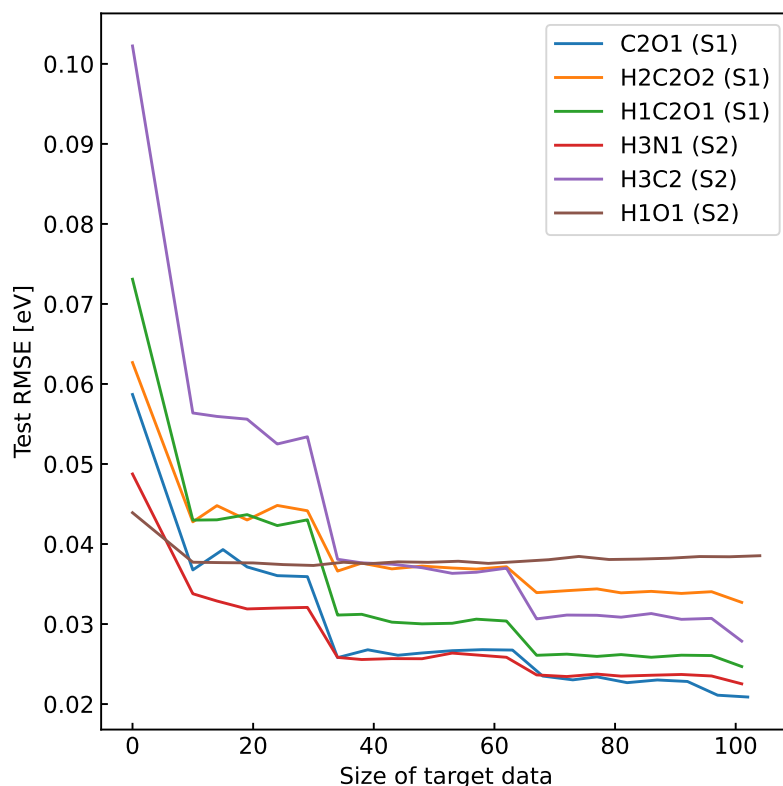


**Figure 11.** Test error as a function of the size of training target data with different sources.

- **Efficient sampling from ensemble:** With the source data preparation, the ensemble average is most expensive part and could be a bottleneck of this method. For efficient data production, high-throughput computational frameworks for surface structures and molecular adsorption are available [58, 22]. Alternatively, it would be a promising direction using a surrogate model for the adsorption energy [59].
- **Expansion of chemical space coverage:** The obvious drawback of this approach is the need for diverse target data, even in small quantities. Related to the previous point, it is required to define domain transformations that cover the global chemical space. For example, evaluation of prediction uncertainty and Bayesian search for the next experiments could be used to expand the coverage efficiently.
- **Optimal design of conversion function:** The performance of the proposed method is highly dependent on the form of  $F$  and the strategy of source selection. Since there is a trade-off between function capacity and trainability,  $F$  should be designed appropriately for the target task and the available data. Although this demonstration used a simple linear scaling function, it cannot work beyond the scope of the underlying Brønsted–Evans–Polanyi relation holding on a limited range of adsorption energy [30]. Future work could explore more representative functions

such as a piecewise linear function or a more complex volcano-like function to capture the global trend in catalysis known as the Sabatier principle [54].

- **Composing multiple sources:** In this study, one source data was selected and used for transition training. However, in actual catalysis, activation energies and corresponding molecules are not uniquely determined either, since rate-limiting processes generally differ depending on the substance and surface [52]. To deal with this situation, it is promising to use more flexible methods in function estimation or domain transformation, for instance, importance weighting per source or per instance [46].
- **Refinement of the prediction model:** The current demonstration tested a simple parameter transfer framework for the prediction model. As the next step, the model architecture and the training strategy could be further optimised for the target task. Since any method that supports homogeneous domain adaptation can be applied here, we could explore not only different architectures but also different algorithms.

## 5. Conclusions

In this work, we proposed a simulation-to-real (Sim2Real) transfer learning method from first-principles data to experimental data based on the chemistry-informed domain transformation. The central problem addressed in this work is the domain difference between computational and experimental data, the former describes a microscopic picture of a material and the latter a macroscopic one. The proposed method first transforms the source computational domain into the target experimental domain and then performs homogeneous domain adaptation to construct a prediction model for the target task. The domain transformation is achieved by the knowledge-based hypotheses on the statistical ensemble and the conversion function, which are designed to reflect the underlying chemical laws and enable linking qualitatively different features and physical quantities.

As a proof of concept, we demonstrated the effectiveness of the proposed method in the prediction task of catalyst activity for the reverse water-gas shift reaction. Using the *Open Catalyst 2020* [22], a large first-principles dataset, as the source dataset and the high-throughput experimental dataset from Wang *et al.* [9] as the target dataset, we construct a prediction model for the activation energy.

Through a verification with dummy target data and a demonstration with the experimental data, we confirmed that the proposed method shows positive transfer of increasing accuracy and data efficiency compared to the model trained only with target data. The test losses of transferred model was approximately one order of magnitude smaller than that of full scratch model. Moreover, the source model has already been optimized in the target space, despite only using less than 10 target data during the domain transformation.

In conclusion, our proposed method helps to significantly reduce the number of experiments in real laboratories, leading to a drastic reduction of the cost and time of exploring novel materials. Finally, the essence of this approach is to integrate the four scientific paradigms, experiment, theory, computation, and data, thereby allowing full use of every possible knowledge. We believe that this work paves the way for the scheme of theory-informed transfer learning between computation and experiment, which should be effective for a variety of materials and tasks.

## Acknowledgement

We would thank Masahiko Ishida and Masato Hiroshima in NEC corporation, Japan for useful comments. We would also thank Yuya Ono in National Institute of Advanced Industrial Science and Technology, Japan for fruitful discussions. This work was supported by Grants-in-Aid from the Japan Society for the Promotion of Science (JSPS) for Scientific Research (KAKENHI grant nos. 20K19871 and 24K20836 to K.M.).

## References

- [1] Tony Hey. *The fourth paradigm: Data-intensive scientific discovery*. Microsoft Research, October 2009.
- [2] Jing Wei, Xuan Chu, Xiang-Yu Sun, Kun Xu, Hui-Xiong Deng, Jigen Chen, Zhongming Wei, and Ming Lei. Machine learning in materials science. *InfoMat*, 1(3):338–358, September 2019.
- [3] Teng Zhou, Zhen Song, and Kai Sundmacher. Big data creates new opportunities for materials research: A review on methods and applications of machine learning for materials design. *Engineering (Beijing)*, 5(6):1017–1026, December 2019.
- [4] Gabriel R Schleder, Antonio C M Padilha, Carlos Mera Acosta, Marcio Costa, and Adalberto Fazzio. From DFT to machine learning: recent approaches to materials science—a review. *JPhys Mater.*, 2(3):032001, July 2019.
- [5] Seyed Mohamad Moosavi, Kevin Maik Jablonka, and Berend Smit. The role of machine learning in the understanding and design of materials. *J. Am. Chem. Soc.*, 142(48):20273–20287, November 2020.
- [6] Thanh Nhat Nguyen, Thuy Tran Phuong Nhat, Ken Takimoto, Ashutosh Thakur, Shun Nishimura, Junya Ohyama, Itsuki Miyazato, Lauren Takahashi, Jun Fujima, Keisuke Takahashi, and Toshiaki Taniike. High-throughput experimentation and catalyst informatics for oxidative coupling of methane. *ACS Catal.*, 10(2):921–932, January 2020.
- [7] Kanami Sugiyama, Thanh Nhat Nguyen, Sunao Nakanowatari, Itsuki Miyazato, Toshiaki Taniike, and Keisuke Takahashi. Direct design of catalysts in oxidative coupling of methane via high-throughput experiment and deep learning. *ChemCatChem*, 13(3):952–957, February 2021.
- [8] Sunao Nakanowatari, Thanh Nhat Nguyen, Hiroki Chikuma, Aya Fujiwara, Kalaivani Seenivasan, Ashutosh Thakur, Lauren Takahashi, Keisuke Takahashi, and Toshiaki Taniike. Extraction of catalyst design heuristics from random catalyst dataset and their utilization in catalyst development for oxidative coupling of methane. *ChemCatChem*, 13(14):3262–3269, July 2021.
- [9] Gang Wang, Shinya Mine, Duotian Chen, Yuan Jing, Kah Wei Ting, Taichi Yamaguchi, Motoshi Takao, Zen Maeno, Ichigaku Takigawa, Koichi Matsushita, Ken-Ichi Shimizu, and Takashi Toyao. Accelerated discovery of multi-elemental reverse water-gas shift catalysts using extrapolative machine learning approach. *Nat. Commun.*, 14(1):5861, September 2023.
- [10] Jehad Abed, Jiheon Kim, Muhammed Shuaibi, Brook Wander, Boris Duijf, Suhas Mahesh, Hyeonseok Lee, Vahe Gharakhanyan, Sjoerd Hoogland, Erdem Irtem, Janice Lan, Niels



- Schouten, Anagha Usha Vijayakumar, Jason Hattrick-Simpers, John R Kitchin, Zachary W Ulissi, Aaike van Vugt, Edward H Sargent, David Sinton, and C Lawrence Zitnick. Open catalyst experiments 2024 (OCx24): Bridging experiments and computational models. *arXiv [cond-mat.mtrl-sci]*, November 2024.
- [11] I Takeuchi, O O Famodu, J C Read, M A Aronova, K-S Chang, C Craciunescu, S E Lofland, M Wuttig, F C Wellstood, L Knauss, and A Orozco. Identification of novel compositions of ferromagnetic shape-memory alloys using composition spreads. *Nat. Mater.*, 2(3):180–184, March 2003.
- [12] Hideomi Koinuma and Ichiro Takeuchi. Combinatorial solid-state chemistry of inorganic materials. *Nat. Mater.*, 3(7):429–438, July 2004.
- [13] Ken-Ichi Uchida, Michiko Sasaki, Yuya Sakuraba, Ryo Iguchi, Shunsuke Daimon, Eiji Saitoh, and Masahiro Goto. Combinatorial investigation of spin-orbit materials using spin peltier effect. *Sci. Rep.*, 8(1):16067, October 2018.
- [14] Yuma Iwasaki, Masahiko Ishida, and Masayuki Shirane. Predicting material properties by integrating high-throughput experiments, high-throughput ab-initio calculations, and machine learning. *Sci. Technol. Adv. Mater.*, 21(1):25–28, January 2020.
- [15] Alfred Ludwig. Discovery of new materials using combinatorial synthesis and high-throughput characterization of thin-film materials libraries combined with computational methods. *Npj Comput. Mater.*, 5(1):1–7, July 2019.
- [16] Ryota Shimizu, Shigeru Kobayashi, Yuki Watanabe, Yasunobu Ando, and Taro Hitosugi. Autonomous materials synthesis by machine learning and robotics. *APL Mater.*, 8(11):111110, November 2020.
- [17] B P MacLeod, F G L Parlane, T D Morrissey, F Häse, L M Roch, K E Dettelbach, R Moreira, L P E Yunker, M B Rooney, J R Deeth, V Lai, G J Ng, H Situ, R H Zhang, M S Elliott, T H Haley, D J Dvorak, A Aspuru-Guzik, J E Hein, and C P Berlinguette. Self-driving laboratory for accelerated discovery of thin-film materials. *Sci. Adv.*, 6(20):eaaz8867, May 2020.
- [18] Nathan J Szymanski, Bernardus Rendy, Yuxing Fei, Rishi E Kumar, Tanjin He, David Milsted, Matthew J McDermott, Max Gallant, Ekin Dogus Cubuk, Amil Merchant, Haegyeom Kim, Anubhav Jain, Christopher J Bartel, Kristin Persson, Yan Zeng, and Gerbrand Ceder. An autonomous laboratory for the accelerated synthesis of novel materials. *Nature*, 624(7990):86–91, December 2023.
- [19] Stefano Curtarolo, Gus L W Hart, Marco Buongiorno Nardelli, Natalio Mingo, Stefano Sanvito, and Ohad Levy. The high-throughput highway to computational materials design. *Nat. Mater.*, 12(3):191–201, March 2013.
- [20] Motoaki Nishijima, Takuya Ootani, Yuichi Kamimura, Toshitsugu Sueki, Shogo Esaki, Shunsuke Murai, Koji Fujita, Katsuhisa Tanaka, Koji Ohira, Yukinori Koyama, and Isao Tanaka. Accelerated discovery of cathode materials with prolonged cycle life for lithium-ion battery. *Nat. Commun.*, 5(1):4553, August 2014.
- [21] Yuma Iwasaki, Ryohto Sawada, Eiji Saitoh, and Masahiko Ishida. Machine learning autonomous identification of magnetic alloys beyond the slater-pauling limit. *Commun. Mater.*, 2(1):1–7, March 2021.
- [22] Lowik Chanussot, Abhishek Das, Siddharth Goyal, Thibaut Lavril, Muhammed Shuaibi, Morgane Riviere, Kevin Tran, Javier Heras-Domingo, Caleb Ho, Weihua Hu, Aini Palizhati, Anuroop Sriram, Brandon Wood, Junwoong Yoon, Devi Parikh, C Lawrence Zitnick, and Zachary Ulissi. Open catalyst 2020 (OC20) dataset and community challenges. *ACS Catal.*, 11(10):6059–6072, May 2021.
- [23] Yoshihiro Hayashi, Junichiro Shiomi, Junko Morikawa, and Ryo Yoshida. RadonPy: automated physical property calculation using all-atom classical molecular dynamics simulations for polymer informatics. *Npj Comput. Mater.*, 8(1):1–15, November 2022.
- [24] Richard Tran, Janice Lan, Muhammed Shuaibi, Brandon M Wood, Siddharth Goyal, Abhishek Das, Javier Heras-Domingo, Adeesh Kolluru, Ammar Rizvi, Nima Shoghi, Anuroop Sriram, Félix

- Therrien, Jehad Abed, Oleksandr Voznyy, Edward H Sargent, Zachary Ulissi, and C Lawrence Zitnick. The open catalyst 2022 (OC22) dataset and challenges for oxide electrocatalysts. *ACS Catal.*, 13(5):3066–3084, March 2023.
- [25] Jakub Železný, Yuta Yahagi, Carles Gomez-Olivella, Yang Zhang, and Yan Sun. High-throughput study of the anomalous hall effect. *Npj Comput. Mater.*, 9(1):1–8, August 2023.
- [26] Kristinn Kristinsson and Guy Albert Dumont. System identification and control using genetic algorithms. *IEEE Transactions on Systems, Man, and Cybernetics*, 22(5):1033–1046, 1992.
- [27] Mei Wang and Weihong Deng. Deep visual domain adaptation: A survey. *Neurocomputing*, 312:135–153, 2018.
- [28] Konstantinos Bousmalis, Alex Irpan, Paul Wohlhart, Yunfei Bai, Matthew Kelcey, Mrinal Kalakrishnan, Laura Downs, Julian Ibarz, Peter Pastor, Kurt Konolige, et al. Using simulation and domain adaptation to improve efficiency of deep robotic grasping. In *2018 IEEE international conference on robotics and automation (ICRA)*, pages 4243–4250. IEEE, 2018.
- [29] Joshua P Tobin. *Real-world robotic perception and control using synthetic data*. UC Berkeley, PhD thesis, 2019.
- [30] Ali Hussain Motagamwala and James A Dumesic. Microkinetic modeling: A tool for rational catalyst design. *Chem. Rev.*, 121(2):1049–1076, January 2021.
- [31] Hidetoshi Shimodaira. Improving predictive inference under covariate shift by weighting the log-likelihood function. *J. Stat. Plan. Inference*, 90(2):227–244, October 2000.
- [32] Joaquin Quionero-Candela, Masashi Sugiyama, A Schwaighofer, and Neil D Lawrence. *Dataset Shift in Machine Learning*. Neural Information Processing series. MIT Press, London, England, December 2008.
- [33] Dipendra Jha, Kamal Choudhary, Francesca Tavazza, Wei-Keng Liao, Alok Choudhary, Carelyn Campbell, and Ankit Agrawal. Enhancing materials property prediction by leveraging computational and experimental data using deep transfer learning. *Nat. Commun.*, 10(1):5316, November 2019.
- [34] Stephen Wu, Yukiko Kondo, Masa-Aki Kakimoto, Bin Yang, Hironao Yamada, Isao Kuwajima, Guillaume Lambard, Kenta Hongo, Yibin Xu, Junichiro Shiomi, Christoph Schick, Junko Morikawa, and Ryo Yoshida. Machine-learning-assisted discovery of polymers with high thermal conductivity using a molecular design algorithm. *Npj Comput. Mater.*, 5(1):1–11, June 2019.
- [35] Herim Han and Sunghwan Choi. Transfer learning from simulation to experimental data: NMR chemical shift predictions. *J. Phys. Chem. Lett.*, 12(14):3662–3668, April 2021.
- [36] Florence H Vermeire and William H Green. Transfer learning for solvation free energies: From quantum chemistry to experiments. *Chem. Eng. J.*, 418(129307):129307, August 2021.
- [37] Yuta Aoki, Stephen Wu, Teruki Tsurimoto, Yoshihiro Hayashi, Shunya Minami, Okubo Tadamichi, Kazuya Shiratori, and Ryo Yoshida. Multitask machine learning to predict polymer–solvent miscibility using Flory–Huggins interaction parameters. *Macromolecules*, July 2023.
- [38] Yosuke Harashima, Keiichi Tamai, Shotaro Doi, Munehisa Matsumoto, Hisazumi Akai, Naoki Kawashima, Masaaki Ito, Noritsugu Sakuma, Akira Kato, Tetsuya Shoji, and Takashi Miyake. Data assimilation method for experimental and first-principles data: Finite-temperature magnetization of (nd,pr,la,ce)<sub>2</sub>(fe,co,ni)<sub>14</sub>B. *Phys. Rev. Mater.*, 5(1), January 2021.
- [39] Justin S Smith, Benjamin T Nebgen, Roman Zubatyuk, Nicholas Lubbers, Christian Devereux, Kipton Barros, Sergei Tretiak, Olexandr Isayev, and Adrian E Roitberg. Approaching coupled cluster accuracy with a general-purpose neural network potential through transfer learning. *Nat. Commun.*, 10(1):2903, July 2019.
- [40] Shenghong Ju, Ryo Yoshida, Chang Liu, Stephen Wu, Kenta Hongo, Terumasa Tadano, and Junichiro Shiomi. Exploring diamondlike lattice thermal conductivity crystals via feature-based transfer learning. *Phys. Rev. Mater.*, 5(5):053801, May 2021.
- [41] Eunjae Shim, Joshua A Kammeraad, Ziping Xu, Ambuj Tewari, Tim Cernak, and Paul M Zimmerman. Predicting reaction conditions from limited data through active transfer learning. *Chem. Sci.*, 13(22):6655–6668, June 2022.

- [42] Zhongkai Hao, Songming Liu, Yichi Zhang, Chengyang Ying, Yao Feng, Hang Su, and Jun Zhu. Physics-informed machine learning: A survey on problems, methods and applications. *arXiv [cs.LG]*, November 2022.
- [43] Rajat Arora, Pratik Kakkar, Biswadip Dey, and Amit Chakraborty. Physics-informed neural networks for modeling rate- and temperature-dependent plasticity. *arXiv [cond-mat.mtrl-sci]*, January 2022.
- [44] Gabriel Bradford, Jeffrey Lopez, Jurgis Ruza, Michael A Stolberg, Richard Osterude, Jeremiah A Johnson, Rafael Gomez-Bombarelli, and Yang Shao-Horn. Chemistry-informed machine learning for polymer electrolyte discovery. *ACS Cent. Sci.*, 9(2):206–216, February 2023.
- [45] Nicholas Ballard, Jon Larrañaga, Kiarash Farajzadehahary, and José M Asua. Polymer chemistry informed neural networks (PCINNs) for data-driven modelling of polymerization processes. *Polym. Chem.*, 15(44):4580–4590, November 2024.
- [46] Masashi Sugiyama, Taiji Suzuki, and Takafumi Kanamori. *Density Ratio Estimation in Machine Learning*. Cambridge University Press, February 2012.
- [47] Tongtong Fang, Nan Lu, Gang Niu, and Masashi Sugiyama. Rethinking importance weighting for deep learning under distribution shift. *Advances in neural information processing systems*, 33:11996–12007, 2020.
- [48] Yolanda A Daza and John N Kuhn. CO<sub>2</sub> conversion by reverse water gas shift catalysis: comparison of catalysts, mechanisms and their consequences for CO<sub>2</sub> conversion to liquid fuels. *RSC Adv.*, 6(55):49675–49691, May 2016.
- [49] Miriam González-Castaño, Bogdan Dorneanu, and Harvey Arellano-García. The reverse water gas shift reaction: a process systems engineering perspective. *React. Chem. Eng.*, 6(6):954–976, 2021.
- [50] David Sholl and Janice A Steckel. *Density functional theory: A practical introduction*. Wiley-Blackwell, Hoboken, NJ, March 2009.
- [51] J K Norskov, T Bligaard, A Logadottir, S Bahn, L B Hansen, M Bollinger, H Bengaard, B Hammer, Z Sljivancanin, M Mavrikakis, Y Xu, S Dahl, and C J H Jacobsen. Universality in heterogeneous catalysis. *J. Catal.*, 209(2):275–278, July 2002.
- [52] Ergys Pahija, Christopher Panaritis, Sergey Gusarov, Jalil Shadbahr, Farid Bensebaa, Gregory Patience, and Daria Camilla Boffito. Experimental and computational synergistic design of cu and fe catalysts for the reverse water–gas shift: A review. *ACS Catal.*, 12(12):6887–6905, June 2022.
- [53] Angela M Wood, Ian R White, and Patrick Royston. How should variable selection be performed with multiply imputed data? *Stat. Med.*, 27(17):3227–3246, July 2008.
- [54] Jun Cheng, P Hu, Peter Ellis, Sam French, Gordon Kelly, and C Martin Lok. Bronsted-evans-polanyi relation of multistep reactions and volcano curve in heterogeneous catalysis. *J. Phys. Chem. C*, 112(5):1308–1311, February 2008.
- [55] Gabriel Peyré, Marco Cuturi, et al. Computational optimal transport: With applications to data science. *Foundations and Trends® in Machine Learning*, 11(5-6):355–607, 2019.
- [56] Chang Liu, Erina Fujita, Yukari Katsura, Yuki Inada, Asuka Ishikawa, Ryuji Tamura, Kaoru Kimura, and Ryo Yoshida. Machine learning to predict quasicrystals from chemical compositions. *Adv. Mater.*, 33(36):e2102507, September 2021.
- [57] Adam Paszke, Sam Gross, Francisco Massa, Adam Lerer, James Bradbury, Gregory Chanan, Trevor Killeen, Zeming Lin, Natalia Gimelshein, Luca Antiga, Alban Desmaison, Andreas Köpf, Edward Yang, Zach DeVito, Martin Raison, Alykhan Tejani, Sasank Chilamkurthy, Benoit Steiner, Lu Fang, Junjie Bai, and Soumith Chintala. PyTorch: An imperative style, high-performance deep learning library. *arXiv [cs.LG]*, December 2019.
- [58] Joseph H Montoya and Kristin A Persson. A high-throughput framework for determining adsorption energies on solid surfaces. *Npj Comput. Mater.*, 3(1):1–4, March 2017.
- [59] Janice Lan, Aini Palizhati, Muhammed Shuaibi, Brandon M Wood, Brook Wander, Abhishek Das, Matt Uyttendaele, C Lawrence Zitnick, and Zachary W Ulissi. AdsorbML: a leap in

efficiency for adsorption energy calculations using generalizable machine learning potentials. *npj Computational Materials*, 9(1):1–9, September 2023.

- [60] Guolin Ke, Qi Meng, Thomas Finley, Taifeng Wang, Wei Chen, Weidong Ma, Qiwei Ye, and Tie-Yan Liu. LightGBM: A highly efficient gradient boosting decision tree. *Advances in Neural Information Processing Systems*, 30, 2017.

## Appendix A. Dataset preparation

In this work, we use the *Open Catalyst 2020 (OC20)* [22] for a source computational dataset. For a target experimental dataset, we use the *Wang2023* data provided by Wang *et al.* [9] or the dummy (pseudo-labeled) dataset generated from it.

### Appendix A.1. Open Catalyst 2020

*OC20* is a set of simulated data on molecular adsorption processes at metal surfaces, obtained by first-principles calculations based on the DFT. It randomly samples alloy surfaces within a low-index plane and adsorbs various molecules on them. While it consists of several tasks, we particularly focus on the initial structure to relaxed energy (IS2IR) dataset because we are interested in the adsorption energy. IS2IR is a large collection of pairs of slab structures  $S$  and adsorption energies  $E^M$  per adsorbate  $M$ , including approximately  $10^6$  entries ( $\sim 10000$  surfaces  $\times$  48 molecules). We express these multiple source datasets as  $\{\mathcal{D}^{S(M)}\}_M^{48}$  with  $\mathcal{D}^{S(M)} \equiv \{(x_i^{S(M)}, y_i^{S(M)})\}_{i=1}^{\sim 10000}$ .

### Appendix A.2. Wang2023

Regarding a target dataset, we refer to a high-throughput experimental dataset opened by Wang *et al.* [9]. Their dataset presents measured data on the activity of RWGS on Pt-based catalysts synthesized on TiO<sub>2</sub> supports. The catalysts are prepared such that their compositions are Pt(3)/M1( $l_1$ )-M2( $l_2$ )-M3( $l_3$ )-M4( $l_4$ )-M5( $l_5$ )/TiO<sub>2</sub> where  $M_i$  is an element contained in a loading amount  $l_i$  (wt%) with the 3 wt% Pt, on the TiO<sub>2</sub> support. This dataset consists of pairs of loading amount and CO formation rate,  $r_{\text{CO}}$ , and is one of the largest experimental dataset of catalyst with a total of 300 entries (45 initial compositions and 255 compositions obtained by Bayesian search). Here, we disregard compositions including lanthanoids as they exceed the coverage of *OC20*, reducing the entries to 141 (38+103).

For simplicity, we assume that each catalyst is characterized by a chemical composition among  $\{M_i\}$  plus Pt as  $x^T$ . We derive the activation energy  $y^T$  from the CO formation rate using the Arrhenius equation,

$$r_{\text{CO}} = A \exp\left(\frac{y^T}{k_B T}\right), \quad (\text{A.1})$$

where  $T$  is the measurement temperature,  $A$  is called the pre-exponential factor.  $y^T$  is measured in units of eV.

**Table A1.** List of elements considered in the dummy generation.

	Elements
Ordinary elements	Al, Si, Ga, Ge
4d-transition metals	Nb, Mo, Tc, Ru, Rh, Pd
5d-transition metals	Ta, W, Re, Os, Ir

**Table A2.** List of parameters of the LightGBM for generating pseudo-labels.

Parameter	Value
Data sample strategy	bagging
Number of iterations	100
Learning rate	0.1

In this work,  $A$  is represented by the value of Pt(3)/Rb(1)-Ba(1)-Mo(0.6)-Nb(0.2)/TiO<sub>2</sub>, irrespective of composition. Eventually, we obtain the target dataset as  $\mathcal{D}^T \equiv \{(x_i^T, y_i^T)\}_{i=1}^{141}$ .

### Appendix A.3. Dummy data

We generated a large dummy dataset  $\mathcal{D}^{Ta}$  for Pt-containing quaternary alloys Pt( $l_0$ )-M1( $l_1$ )-M2( $l_2$ )-M3( $l_3$ ) from Wang2023. To avoid combination explosions, we limit the constituent elements M1, M2, and M3 to those listed in the Table A1. In addition, we only consider the compositions with  $l_i \leq 3$ .

First, a prediction model  $\hat{h}$  trained by Wang2023 is prepared. Because only  $\mathcal{D}^T$  is not enough to train with a neural network-based model, we here employ  $\hat{h}$  as a gradient boosting decision tree model implemented in LightGBM code [60]. To train the model, compositions are converted into the XenonPy descriptor (See Appendix. Appendix B). The essential parameters are listed in Table A2.

The dummy generation method is explained in Algorithm 3. In this process, all possible compositions Pt( $l_0$ )-M1( $l_1$ )-...-M <sub>$n_{\text{elem}}$</sub> ( $l_{n_{\text{elem}}}$ ) satisfying  $l_i \leq l_{\text{max}}$  are generated combinatorially. Running it with  $n_{\text{elem}} = 3$  and  $l_{\text{max}} = 3$ , we finally obtain 38674 dummy data.

## Appendix B. Composition featurizer

The XenonPy compositional featurizer is a tool within the XenonPy library that converts raw chemical composition data into informative numerical descriptors suitable for machine learning [56]. It can calculate 290 compositional features for a given chemical composition. This calculation uses the information of the 58 elemental properties. Using weights of each element in a composition, the 290 compositional descriptors are obtained from the five calculations, weighted sum, weighted average, weighted variance,

**Algorithm 3:** Process of the dummy data generation.

---

**Input:**  $\hat{h}$ : Prediction model trained by original target data,  $\mathcal{E}$ : List of elements.

**Output:**  $\mathcal{D}^{\text{Td}}$ : Dummy data.

**parameter:**  $n_{\text{elem}}$ : Number of constituents,  $l_{\text{max}}$ : Maximum composition index

```

1 begin
2    $\mathcal{D}^{\text{Td}} \leftarrow \emptyset$ ;
3   for  $M = (M_1, \dots, M_{n_{\text{elem}}})$  in  $\mathcal{E}^{n_{\text{elem}}}$  do
4     for  $l = (l_0, l_1, \dots, l_{n_{\text{elem}}})$  in  $\{1, \dots, l_{\text{max}}\}^{n_{\text{elem}}+1}$  do
5       if  $\text{GCD}(l) == 1$  then
6          $x_{\text{new}} \leftarrow \text{Pt}(l_0) - M_1(l_1) - \dots - M_{n_{\text{elem}}}(l_{n_{\text{elem}}})$ ;
7          $z_{\text{new}} \leftarrow \text{CompositionalFeaturizer}(x_{\text{new}})$   $y_{\text{new}} \leftarrow \hat{h}(z_{\text{new}})$ ;
8         Append  $(x_{\text{new}}, y_{\text{new}})$  to  $\mathcal{D}^{\text{Td}}$ ;
9   return  $\mathcal{D}^{\text{Td}}$ ;

```

---

max-pooling, and min-pooling, on the 58 elemental properties ( $58 \times 5 = 290$ ). For more detail, see the code repository.

In this work, since all  $f$ -block elements are excluded from our datasets in advance, we ignore `num_f_unfilled` and `num_f_valence` out of the 58 elemental properties. Moreover, we omit the `weighted sum` calculation as it is identical to the `weighted average` for a periodic system. Consequently, we use  $56 \times 4 = 224$  descriptors.

## Appendix C. Experimental details

### Appendix C.1. Function estimation

Figure C1 show the regression lines for each sources selected from strategy S1 with *Wang2023* target data. That from the strategy S2 has been already shown in Figure 6.

The numerical values in the linear scaling lines are provided in Table C1

While the main text only showed the function estimation for *Wang2023* dataset, here we show the results for the dummy dataset. The result of source selection with Algorithm. 2 for the dummy data is shown in Figure C2.

The linear scaling lines between the dummy activation energy and the adsorption energies for each strategy are provided in Figures C3 and C4. The numerical values are shown in Table C2.

### Appendix C.2. Source training

All essential parameters through our experiments are summarized in Table C3.

Figure Appendix C.2 shows training curves with source data, displaying the mean and the standard deviation of losses obtained by 10-fold cross validation. The result

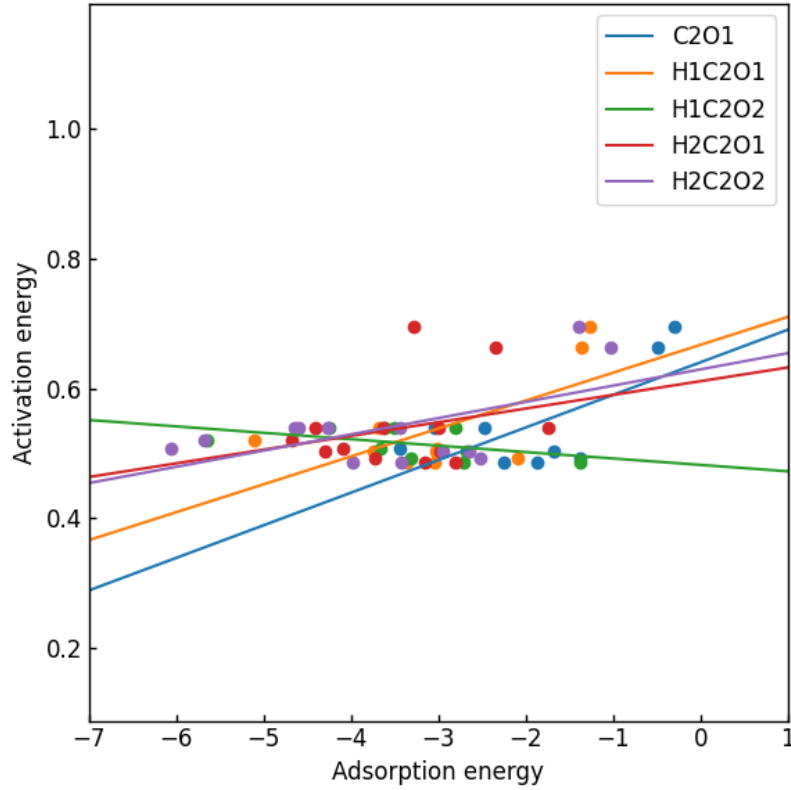


**Figure C1.** Linear scaling between activation energy and adsorption energies for each sources from strategy S1.

**Table C1.** Numerical values of the linear scaling for each source.

Source	Strategy	a	b
C2O1	S1	0.05016	0.64007
H1C2O1	S1	0.04293	0.66702
H1C2O2	S1	-0.00987	0.48225
H2C2O1	S1	0.02107	0.61106
H2C2O2	S1	0.02499	0.62920
H3N1	S2	0.14285	0.78651
H3C2	S2	0.06510	0.77389
H1N1O1	S2	0.01590	0.55576
H5C2O2	S2	0.02596	0.63037
H1O1	S2	0.14461	0.66663
H3C1	S2	0.09692	0.77077
H3C2O1	S2	0.06735	0.79618

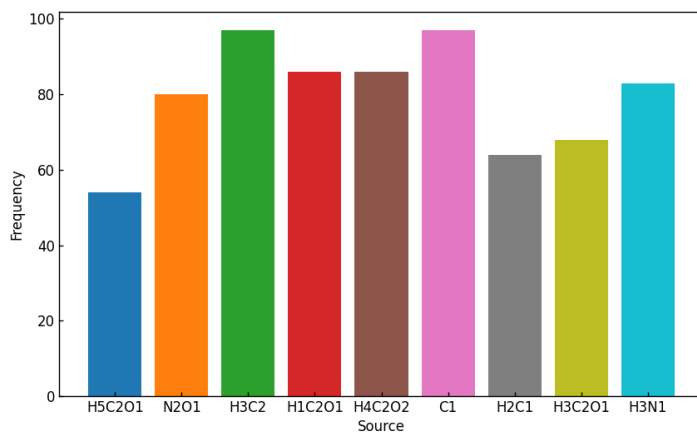


**Figure C2.** Results of source selection with strategy S2 for dummy data.

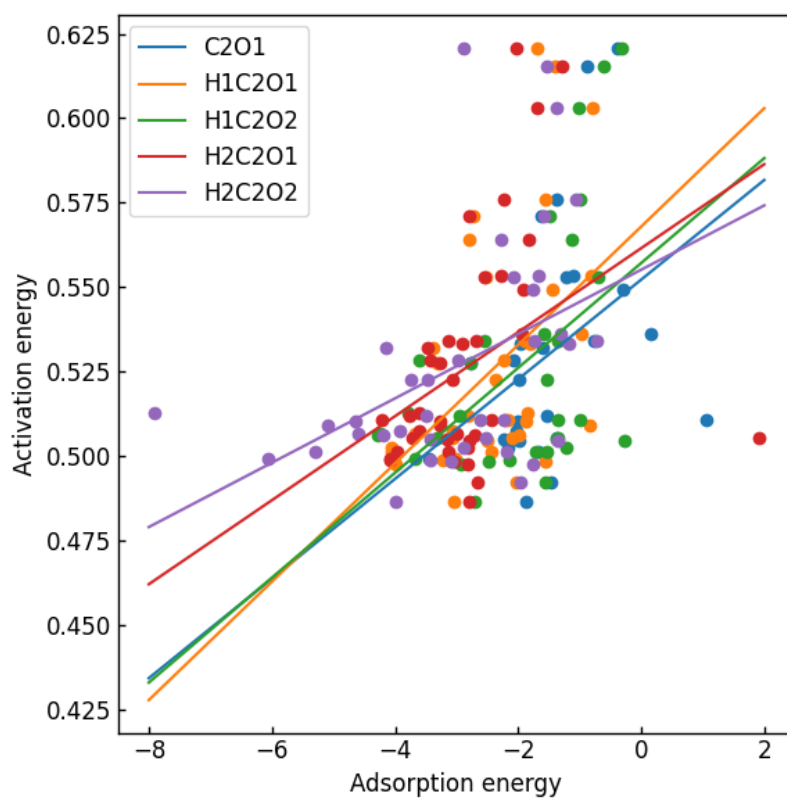


**Figure C3.** Linear scaling between dummy activation energy and adsorption energies for each sources from strategy S1.



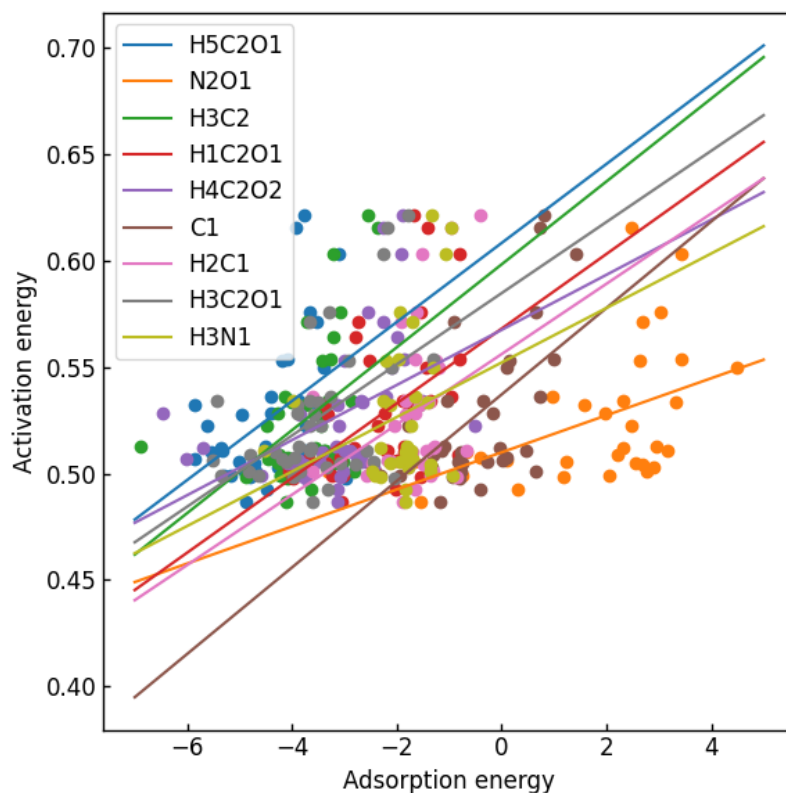


**Figure C4.** Linear scaling between dummy activation energy and adsorption energies for each sources from strategy S2.

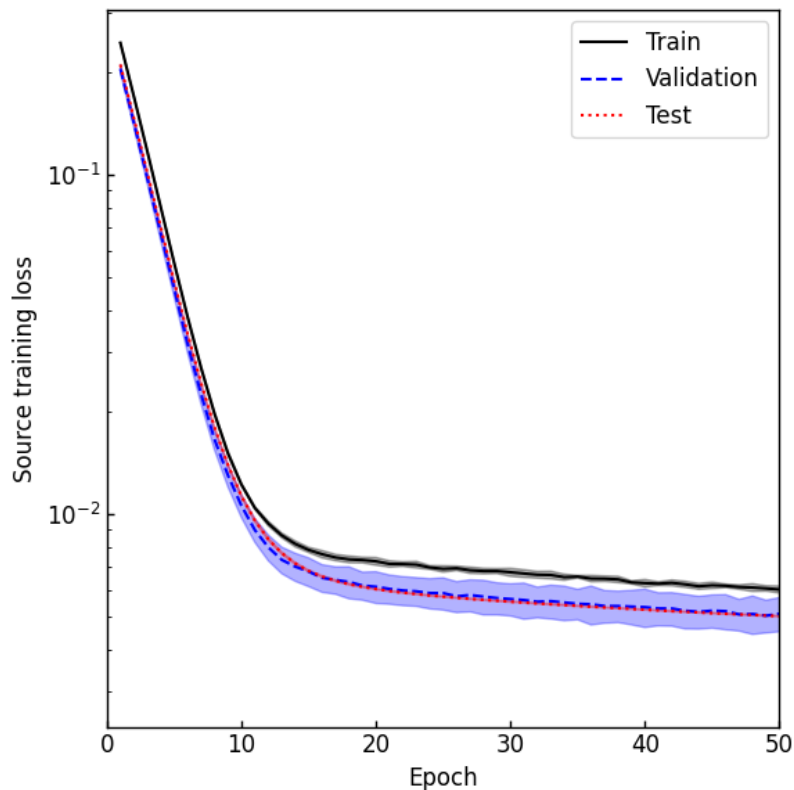
**Table C2.** Coefficients and intercepts for each regression lines.

Source	Strategy	a	b
C2O1	S1	0.01474	0.55223
H1C2O1	S1	0.01751	0.56792
H1C2O2	S1	0.01552	0.55714
H2C2O1	S1	0.01243	0.56153
H2C2O2	S1	0.00952	0.55516
H5C2O1	S2	0.01853	0.60810
N2O1	S2	0.00869	0.50991
H3C2	S2	0.01944	0.59807
H1C2O1	S2	0.01751	0.56792
H4C2O2	S2	0.01292	0.56735
C1	S2	0.02028	0.53705
H2C1	S2	0.01649	0.55598
H3C2O1	S2	0.01669	0.58458
H3N1	S2	0.01278	0.55205

**Table C3.** List of model parameters and experimental conditions of our demonstration.

Parameter	Value
Input dimension	224
Output dimension	1
Training batch size	32
Optimizer	SGD
Learning rate	0.001
Random seed (source pretrain)	0
Random seed (target training)	0
Epochs (source pretrain)	50
Epochs (target training)	175

of C2O1 dataset is shown as an example. Here, we separated the 20% of source data for testing, and performed cross validation with the remaining 80%. Apart from the validation, the source model was trained using all the source data, and carried out early stopping on 50 epochs.

**Figure C5.** Source training curve for C2O1 data with respect to the losses of training, validation, and test, as functions of the number of epochs.

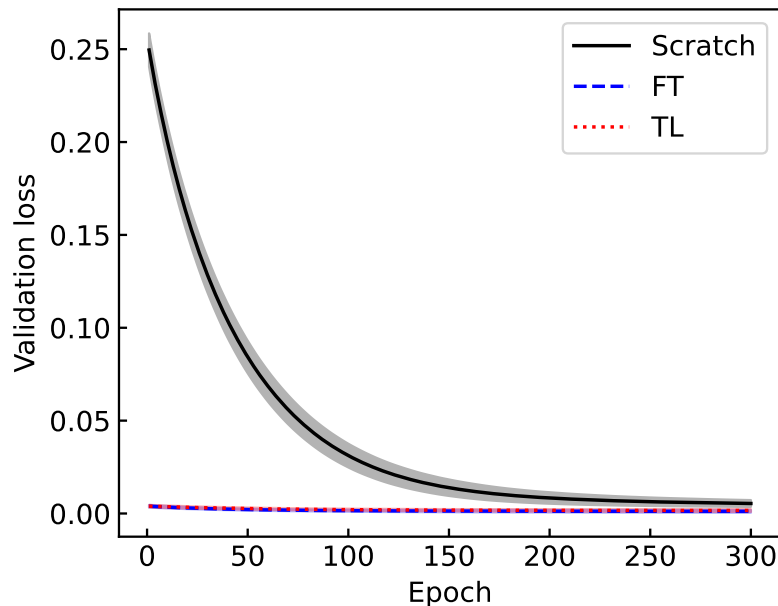


**Figure C6.** Target training curve with respect to the validation losses for each training methods, as functions of the number of epochs.

### Appendix C.3. Target training

Figure Appendix C.3 shows the target training curves for each retraining methods of the full scratch, the fine tuning, and the transfer learning, explained in Section 4.3.5. Here, C2O1 dataset is used as an example. The mean and the standard deviation of validation losses obtained by 10-fold cross validation are displayed. With the prediction models, we stopped training after 125 epochs.

We also performed 10-fold cross validation during the target training with the dummy dataset. Figure C7 shows its target training curve using the C2O1 source data. To compare with the Wang2023 containing 141 target data, we limit the size of dummy data to 200 instances by random sampling. As a result, Figure Appendix C.3 and C7 show similar behavior.

Using full dummy data, we can investigate the behavior of the target training with a large target dataset, as shown in Figure C8. According to the result, the full-scratch and the FT exceed the TL in the case with a large dataset; It is reasonable because the last one has a lesser capacity for fixed parameters than others. However, as show in the main text, there is little difference between FT and TL in the range with  $O(100)$  data, and both are superior to the full-scratch model.

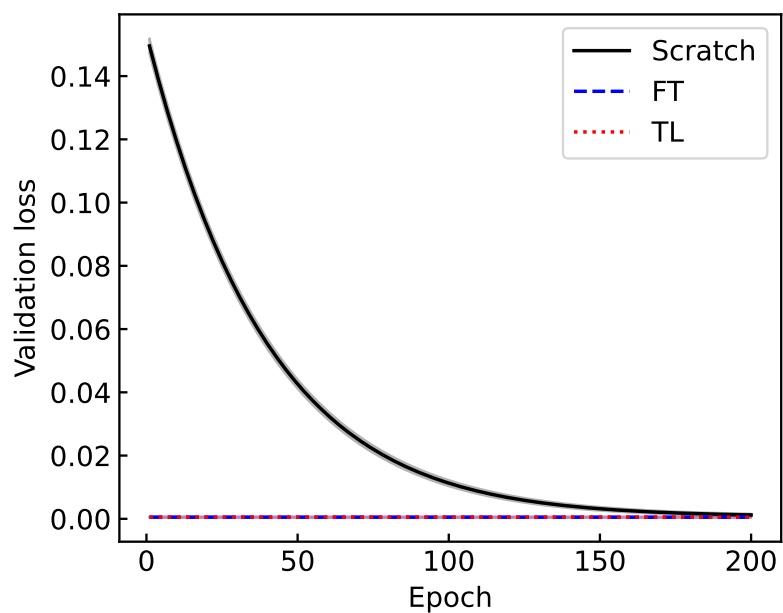


**Figure C7.** Target training curve with the limited (200) dummy data.

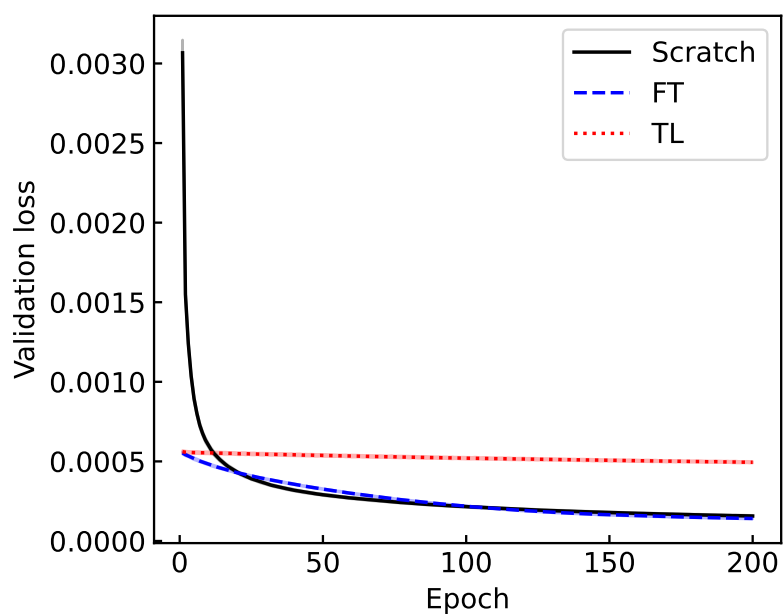


**Figure C8.** Target training curve with the limited (200) dummy data.